White Rose Research Online

eprints@whiterose.ac.uk
https://eprints.whiterose.ac.uk
Universities of Leeds, Sheffield and York

Deposited via The University of Sheffield.

White Rose Research Online URL for this paper:
https://eprints.whiterose.ac.uk/id/eprint/241960/

Version: Accepted Version

Article:
Bidar, O. and Colombo, M. (2026) Evaluations of boiling heat flux partitioning and bubble parameter models using a 0-D framework. International Journal of Heat and Mass Transfer, 269. 129059. ISSN: 0017-9310

https://doi.org/10.1016/j.ijheatmasstransfer.2026.129059

© 2026 The Authors. Except as otherwise noted, this author-accepted version of a journal article published in International Journal of Heat and Mass Transfer is made available via the University of Sheffield Research Publications and Copyright Policy under the terms of the Creative Commons Attribution 4.0 International License (CC-BY 4.0), which permits unrestricted use, distribution and reproduction in any medium, provided the original work is properly cited. To view a copy of this licence, visit http://creativecommons.org/licenses/by/4.0/

Reuse
This article is distributed under the terms of the Creative Commons Attribution (CC BY) licence. This licence allows you to distribute, remix, tweak, and build upon the work, even commercially, as long as you credit the authors for the original work. More information and the full terms of the licence here: https://creativecommons.org/licenses/

Takedown
If you consider content in White Rose Research Online to be in breach of UK law, please notify us by emailing eprints@whiterose.ac.uk including the URL of the record and the reason for the withdrawal request.

UNIVERSITY OF LEEDS
University of Sheffield
UNIVERSITY of York

Highlights

- Zero-dimensional framework developed for systematic testing of boiling closures
- Over 16,000 HFP and bubble parameter model combinations evaluated
- No single boiling closure combination consistently reproduces experimental data
- Sensitivity analyses reveal regime-dependent influence of bubble parameter models
- Structural differences between RPI and MIT models strongly affect heat flux partitioning

Evaluations of boiling heat flux partitioning and bubble parameter models using a 0-D framework

Omid Bidar*, Marco Colombo

School of Mechanical, Aerospace and Civil Engineering, University of Sheffield, Sir Frederick Mappin Building, Mappin Street, Sheffield, S1 3JD, United Kingdom

Abstract

Reliable prediction of boiling heat transfer remains a major challenge in thermal hydraulics due to the complex mechanisms governing phase change at heated surfaces. In this work, we develop a zero-dimensional (0-D), point-averaged framework to systematically evaluate and compare the predictive performance of multiple heat flux partitioning (HFP) formulations and bubble dynamics sub-models. HFP models decompose the total heat transfer into individual components characterising various heat transfer mechanisms, such as evaporation, quenching and single-phase convection. This approach relies on sub-models characterising bubble dynamics parameters such as bubble departure diameter, frequency, and nucleation site density. The framework, implemented in MATLAB as XBOIL, enables rapid and exhaustive testing of thousands of HFP and bubble parameter sub-model combinations. Model predictions are compared against an extensive experimental database covering both pool and flow boiling under a wide range of pressures, mass fluxes, and subcoolings. The approach isolates the role and interactions of individual sub-models, allowing both case-specific and global assessments of accuracy and generalisability. Results reveal that while some sub-models consistently contribute to improved predictive accuracy, no single configuration performs optimally across all conditions, highlighting compensatory effects among various closures involved in modelling boiling heat transfer. Complementary sensitivity analyses are conducted to examine the effects of flow conditions, the sensitivity of modelling parameters such as contact angle, and the influence of different sub-model selections on heat flux predictions.

Keywords: heat flux partitioning, boiling models, flow boiling, pool boiling, multiphase flows

*Corresponding author

Email address: o.bidar@sheffield.ac.uk (Omid Bidar)

1. Introduction

Nucleate boiling is an important process in nuclear thermal hydraulics, and critical heat flux (CHF) remains one of the most important safety limits for water-cooled nuclear reactors. Beyond nuclear systems, boiling processes are also central to many thermal management applications in electronics, energy systems, and aerospace platforms where efficient phase-change heat transfer is desired. However, reliable predictions of heat transfer rates and the CHF remain challenging due to the complexity of the boiling process, the not yet fully understood interaction between the heated surface and the working fluid, and the interplay between multiple variables such as thermophysical properties, operating conditions, and surface chemistry.

In the last few decades, computational fluid dynamics (CFD) models based on the multifluid Eulerian–Eulerian method have been developed to simulate three-dimensional multiphase flows in complex geometries. Example applications of Eulerian-Eulerian multifluid simulations include: nuclear thermal hydraulics [1], nuclear safety demonstration [2], petroleum industry [3], and beyond. Multifluid models are developed by averaging the local and instantaneous velocity and phase distribution. This averaging process filters out the interface position and lengthscale, and interface and turbulent transport and exchange processes must be modelled with numerous closure relations [4, 5].

In Eulerian–Eulerian models, the heat flux partitioning (HFP) approach is commonly used to model the wall boiling process. In the HFP approach, the heat transfer is typically modelled as the sum of several contributing mechanisms, usually evaporation, quenching, and single-phase heat transfer [6]. Fundamental quantities characterising the bubble growth dynamics, such as bubble nucleation site density, departure diameter, departure frequency, wait and growth times, are required to model the evaporation heat transfer mechanism in HFP models. Over the years, a plethora of empirical, semi-empirical, and mechanistic models have been developed to predict these quantities [7]. However, their predictive capabilities are often limited due to the models' inability to capture the complex interdependency between these bubble dynamics quantities that are usually independently modelled, the overfitting of the various model parameters on limited experimental data, and epistemological uncertainties due to incomplete understanding of the underlying flow physics [8, 9, 10].

Over the years, various studies have been conducted to assess the predictive capabilities of various aspects of multifluid CFD models, including assessments of the HFP closure models (e.g. [8, 10]), interfacial area transport modelling (e.g. [11, 12]), bubble coalescence and break-up models (e.g. [12, 13]) and turbulence closures (e.g. [14]). Recently, in a more comprehensive assessment of multiphase CFD modelling of high

pressure boiling flows, benchmark results from 12 participants were published [15], with the results compared against data from the DEBORA experiment [16].

When multi-fluid CFD simulations are used to assess the accuracy of HFP approaches, each closure model (whether it addresses turbulence, interfacial forces, or bubble interactions) contributes its own uncertainties, which can all accumulate and obscure those arising from the boiling model. Even in studies that focus specifically on HFP models, discrepancies attributable to turbulence modelling or interfacial transport may dominate, making it difficult to isolate the behaviour of individual bubble dynamics sub-models. Furthermore, systematically exploring every combination of bubble parameter sub-models is computationally prohibitive in the context of CFD, since the range of possible HFP configurations can yield thousands of distinct simulation scenarios. As a result, most existing studies necessarily restrict their attention to a limited subset of sub-models (boiling-specific closures or otherwise), while the remaining models are either chosen heuristically or kept fixed without evidence that they represent the most appropriate combination. This introduces the risk that reported findings reflect the specific choice of auxiliary sub-models rather than the intrinsic performance of the boiling model formulation.

A complementary, computationally efficient strategy is provided by point-averaged simulations, e.g. [17], wherein boiling phenomena are modelled at a point representative of the heater surface average conditions rather than across a full three-dimensional flow domain. This allows the boiling models to be represented as explicit functions of the wall superheat, bulk flow conditions, characteristic length scale, and fluid and surface thermophysical properties (usually available from experiments), while eliminating the need for iterative solution methods. Although the zero-dimensional (0-D) approach neglects detailed spatio-temporal flow features, it offers a practical and efficient framework for isolating and rapidly testing different boiling HFP methods and sub-models. A typical 3D multiphase simulation may take hours, while point-averaged evaluations complete in milliseconds. Comparing these model predictions against experimental measurements, e.g. via boiling curves, provides a useful pre-screening mechanism for sub-model selection and refinement prior to more expensive CFD efforts.

In addition to their computational efficiency, point-based models enable isolating the role of individual sub-models and their interactions—an essential capability given that HFP models derive their predictions from the tightly coupled contributions of multiple sub-models. A key objective of this study is not only to assess the performance of individual sub-models, but also to quantify how their combinations behave across multiple datasets and conditions. In this paper, we investigate whether certain sub-models consistently contribute to high predictive accuracy, or whether

accurate predictions arise from compensatory effects between imperfect components. We also aim to explore whether any combination achieves robust performance across a wide range of conditions, or whether different scenarios inevitably favour different configurations.

Recent experimental advances now make available increasingly detailed measurements of the boiling heat transfer process. High-resolution imaging methods, coupled with IR thermography, specialised optical diagnostics and advanced post-processing techniques, enable not only the measurement of heat fluxes on surfaces, but also capture fundamental bubble dynamics parameters (e.g. nucleation site density, bubble departure diameters and frequencies) and estimate the individual heat transfer mechanisms [18, 19, 20]. These capabilities allow detailed assessment of HFP-based models beyond overall heat flux, including internal consistency in the modelling of bubble-scale phenomena. Zero-dimensional, point-based models can effectively take advantage of these advanced datasets, which are often acquired in small-scale, controlled experiments not easily addressed with large-scale CFD models.

This study introduces a systematic zero-dimensional (0-D) point-averaged framework for the large-scale assessment of heat flux partitioning (HFP) formulations and bubble dynamics sub-models. By evaluating more than 16,000 possible closure combinations across multiple pool and flow boiling databases, the framework enables controlled comparison of model behaviour independently of turbulence modelling, interfacial transport closures, and mesh-dependent uncertainties inherent to CFD simulations. The objective is not to replace CFD-based boiling solvers, but to establish a computationally efficient environment in which the algebraic structure, cross-compatibility, and sensitivity of HFP and bubble parameter closures can be interrogated rigorously. In conventional multi-fluid CFD studies, uncertainties associated with turbulence modelling, interfacial transport, and other auxiliary closures can obscure the behaviour of the boiling models, while the large number of possible sub-model combinations makes systematic exploration computationally impractical. The present framework overcomes these challenges and the results provide a systematic mapping of closure behaviour across operating regimes, revealing compatibility trends, sensitivity patterns, and structural limitations of existing model combinations under diverse flow conditions.

The rest of the paper is structured as follows: *Section 2* presents the heat flux partitioning and bubble parameter models, and the XBOIL code developed in this work; *Section 3* presents the experimental database curated in this work and the evaluation methodology; *Section 4* presents the evaluation results with in-depth discussions. Finally, *Section 5* summarises key findings and highlights future work.

2. Modelling framework

2.1. Heat flux partitioning and bubble parameter models

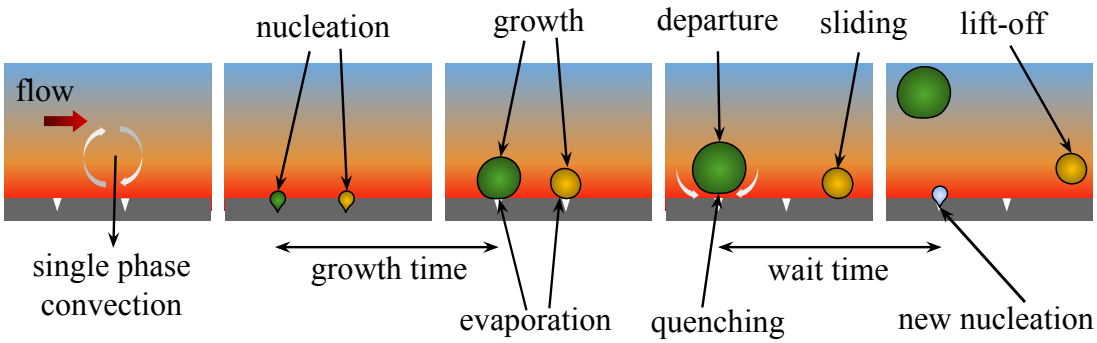

Figure 1: A simplified representation of boiling process illustrating key phenomena and bubble dynamics parameters.

Fig. 1 illustrates the key boiling processes. It begins with nucleation at microscopic cavities on the heated surface, where trapped gas initiates bubble formation once the wall reaches the required amount of superheat. As bubbles nucleate, they grow rapidly, trapping a thin microlayer of liquid against the wall, which evaporates adding to heat transfer. After this initial growth, a dry spot forms under the bubble, and the wall temperature rises locally until the bubble departs. Once the bubble detaches, fresh liquid rewets this area, rapidly cooling it through transient conduction. Depending on conditions, bubbles may either detach directly or slide along the surface before lifting off, with sliding bubbles enhancing heat transfer by disrupting the boundary layer. At high heat fluxes, bubbles interact more frequently, merging or detaching early due to crowding, which alters the heat transfer dynamics. In bubble-free areas, single-phase convection continues, with additional turbulence from surface roughness contributing to heat transfer [21]. HFP models represent these heat transfer mechanisms as individual contributors to the total heat flux.

In practice, modelling these processes requires the specification of multiple interdependent bubble dynamics parameters, including the departure diameter and frequency, nucleation site density, growth time, and wait time. Each of these quantities is coupled to fluid properties, surface characteristics, and operating conditions, and their combined influence determines the balance between the various heating mechanisms being modelled to capture the total heat flux. As illustrated in Fig. 2, the relationships between the sub-models are highly complex. This interconnected-

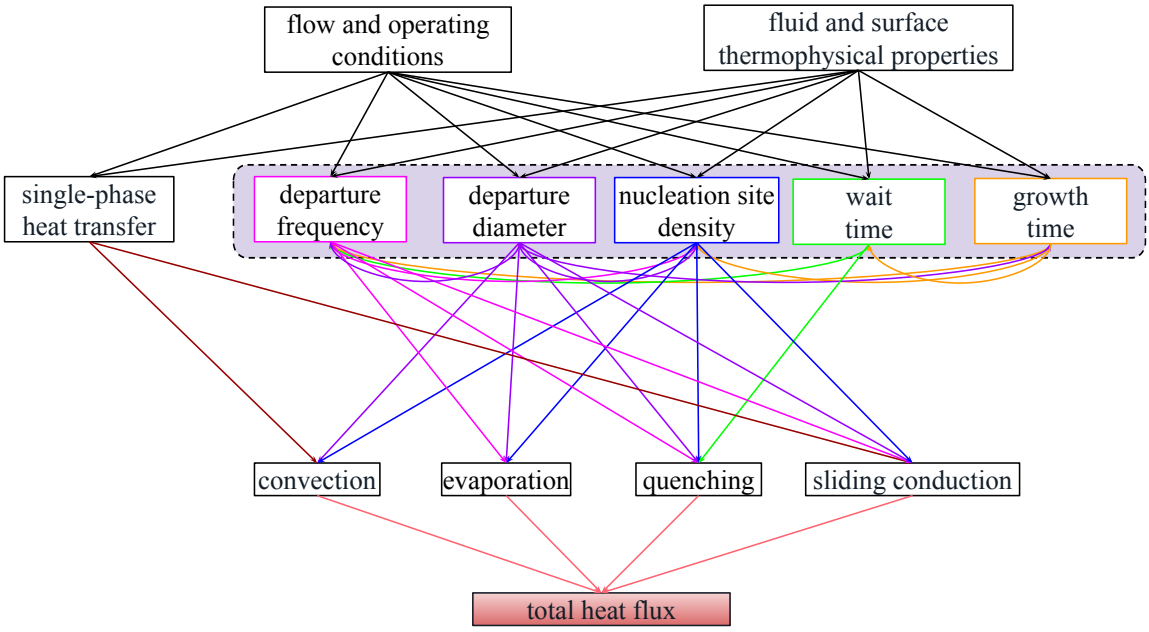

Figure 2: Various components and their interdependencies in heat flux partitioning modelling.

ness underlines the difficulty of identifying universally reliable models and highlights the importance of assessing them systematically in combination rather than isolation.

Mathematically, the total heat flux can be represented as a function of a chosen heat flux partitioning (HFP) framework, $\mathcal{F}_{\text{HFP}}$, which in turn depends on several bubble dynamics parameter sub-models:

$$q''(\Delta T_w) = \mathcal{F}_{\text{HFP}}\left(D_d, f, \overline{N}_b, t_w, t_g, \text{Nu}, \varphi\right), \tag{1}$$

where D_d is the bubble departure diameter, f is the departure frequency, $\overline{N}_b$ is the nucleation site density, t_g is the bubble growth time, t_w is the bubble wait time, Nu is the Nusselt number, and φ represents other flow and thermophysical parameters, such as pressure, subcooling, geometric parameters such as hydraulic diameter, and thermophysical properties of the heating surface and the working fluid. Each HFP formulation prescribes a specific decomposition of the total heat flux, q'', into constituent mechanisms. For example, the widely used RPI model expresses the

total heat flux as

$$\mathcal{F}_{RPI} = q''_{\text{convection}} + q''_{\text{evaporation}} + q''_{\text{quenching}}, \tag{2}$$

$$q''_{\text{convection}} = h_c \left(1 - \frac{\pi}{4} D_d^2 K \overline{N}_b\right) (T_w - T_l), \tag{3}$$

$$q''_{\text{evaporation}} = \frac{\pi}{6} \rho_v h_{lv} D_d^3 f \overline{N}_b, \tag{4}$$

$$q''_{\text{quenching}} = t_w f \frac{\pi}{4} D_d^2 K \overline{N}_b \frac{2k_l (T_w - T_l)}{\sqrt{\pi t_w k_l / \rho_l c_{p,l}}}, \tag{5}$$

where h_c is the single-phase convection heat transfer coefficient (as a function of the Nusselt number); K is the bubble growth constant; ρ_v is the vapour density; h_{lv} is latent heat of vapourisation; k_l is the liquid thermal conductivity; ρ_l is the liquid density, $c_{p,l}$ is the liquid specific heat capacity; T_w and T_l are the wall and liquid temperatures respectively, and calculated as $T_w - T_l = \Delta T_w + \Delta T_{\text{sub}}$, where $\Delta T_w = T_w - T_{\text{sat}}$ is the wall superheat and $\Delta T_{\text{sub}} = T_{\text{sat}} - T_l$ is the subcooling temperature.

The RPI formulation illustrates how wall heat transfer in nucleate boiling is decomposed into contributions from convection, quenching, and evaporation, each governed by subsidiary closure relations. In practice, these closures are drawn from a wide family of sub-models that describe the microscopic mechanisms governing bubble dynamics and wall–fluid interaction. Empirical and semi-empirical formulations remain the most widely used, having been derived from limited parametric datasets and typically correlated with wall superheat, pressure, or surface conditions. More recent developments have introduced mechanistic and semi-mechanistic alternatives that replace purely fitted constants with physically motivated relations, most notably for the bubble departure diameter. Force-balance models, originating from the work of Klausner et al. [22] and later refined by Colombo and Fairweather [23] among others [24], compute the departure diameter by considering the surface-tension, buoyancy, drag, and lift forces acting on a growing bubble, coupled to a growth-rate equation that may account for microlayer evaporation and condensation on the bubble cap. Similarly, newer formulations link the bubble departure frequency and waiting time directly to the predicted growth dynamics, in attempts to improve the internal coherence of the models. Together, these sub-models define the physical fidelity of the heat-flux partitioning framework, and their combined uncertainty remains a key factor in determining the accuracy and generality of boiling flow simulations.

In the present work, we assess various heat flux partitioning and bubble parameter sub-models, see full list in Table 1. Altogether, this allows the assessment of 16,838

distinct configurations, which to our knowledge, is the first attempt of its kind. In the following, each model combination is evaluated systematically within the 0-D framework to quantify both individual and joint effects of these sub-models.

It is important to clarify that the present zero-dimensional framework is not intended to replace an Eulerian–Eulerian CFD wall-boiling simulation. Most boiling closures evaluated in this study (such as correlations for bubble departure diameter, departure frequency, and nucleation site density) are formulated as local algebraic relations that depend primarily on thermodynamic properties and operating conditions, such as wall superheat, liquid subcooling, pressure, and fluid properties. In Eulerian–Eulerian CFD implementations these correlations are evaluated using local quantities obtained from the solution field, for example the liquid temperature in the near-wall cell or heat transfer coefficients derived from wall-function formulations. In the present 0-D framework the same relations are instead evaluated using prescribed thermophysical conditions representative of the experimental cases. The principal difference therefore lies in how these local input quantities (such as the liquid temperature used to determine wall superheat) are obtained. In CFD simulations the surrounding transport problem, including turbulence modelling, wall heat transfer formulations, and multiphase transport, determines the local temperature field and related quantities, which in turn influence the values entering the boiling closures. The 0-D framework removes this additional modelling layer and allows the sensitivities and compatibility of the closures themselves to be examined under controlled conditions. At the same time, most correlations depend only on a limited set of local thermodynamic variables and do not explicitly incorporate any detailed spatial information from the surrounding flow field, meaning that the additional resolution available in CFD does not necessarily translate into additional physical content within the closures themselves. Therefore, while CFD simulations may modify quantitative predictions by altering the local conditions under which the correlations/models are evaluated, the trends identified here primarily reflect structural properties of the closures and remain informative for their use in CFD-based implementations.

Table 1: List of tables outlining the models in each sub-model category. N represents the number of sub-models in each category. The 'Table' column lists the tables where these models are shown with brief descriptions in the Appendix.

Model category	N	Table	Model name	Reference(s)
Heat flux partitioning	3	A1	RPI	[25]
			MIT	[17, 21]

Continued on next page

Table 1 (*Continued*)

Model category	N	Table	Model name	Reference(s)
			Kim & Kim	[26]
Departure diameter	13	A2	Bovard	[27]
			Cole	[28]
			Cole & Rohsenow	[29]
			Colombo & Fairweather	[23]
			Fritz	[30]
			Golorin et al.	[31]
			Kocamustagaogullari	[32]
			MIT	[17]
			Nam	[33]
			Phan	[34]
			Ruckenstein	[35]
			Tolubinsky & Kostanchuk	[36]
			Van Stralen & Zijl	[37]
Departure frequency	6	A3	Cole	[38]
			Exact (by definition)	-
			Peebles & Garber	[39]
			Sakashita & Ono	[40]
			Stephan	[41]
			Zuber	[42]
Nucleation site density	6	A4	Hibiki & Ishii	[43]
			Hibiki–Ishii–MIT	[17]
			Lemmert & Chawla	[44]
			Li et al.	[45]
			Wang & Dhir	[46]
			Yang et al.	[47]
Growth time	3	A5	Lee et al.	[48]
			MIT	[17]
			Van Stralen et al.	[37]
Wait time	2	A5	MIT	[17]
			Van Stralen et al.	[37]
Single-phase convection	2	A6	Churchill & Chu	[49]

Continued on next page

Table 1 (*Continued*)

Model category	N	Table	Model name	Reference(s)
			Gnielinski	[50]

2.2. XBOIL: software implementation and simulation workflow

To enable systematic evaluation of the wide range of heat flux partitioning models and bubble parameter sub-models, we developed a dedicated MATLAB code, referred to as XBOIL (`https://github.com/omid-bidar/XBOIL`). The software is structured around a modular architecture in which each sub-model can be selected independently and used for heat flux predictions. This design allows straightforward extension of the framework by incorporating new sub-models as they become available in the literature.

The inputs to XBOIL are the operating conditions, surface and flow conditions from the experimental datasets, together with a prescribed range of wall superheats. Fluid properties are calculated using CoolProp [51]. For each selected configuration of HFP model and sub-models, the code computes the corresponding bubble parameters. These are then used in the chosen HFP formulation to predict the total heat flux as a function of wall superheat, producing a model boiling curve that can be compared directly against experimental measurements.

A key advantage of XBOIL is computational efficiency. Because the framework is point-averaged and explicitly algebraic, each evaluation completes in milliseconds, enabling exhaustive exploration of the combinatorial model space. For example, a full sweep across tens of thousands of model configurations for all superheat points in a boiling curve can be completed in minutes on a modern multi-core desktop processor. This efficiency makes it feasible to perform not only local evaluations for each case but also global analyses across all datasets, as described in Section 3.2.

3. Experimental datasets and evaluation methodology

3.1. Flow and pool boiling data

To evaluate the predictive capability of the different heat flux partitioning models and bubble dynamics sub-models, a database of both flow boiling and pool boiling experiments has been compiled. The data is mainly in the form of boiling curves, and span a broad range of operating conditions. The datasets are summarised in Tables 2 for flow boiling and Table 3 for pool boiling.

For flow boiling, the database includes nine independent studies covering water and R-134a refrigerant across vertically and horizontally-oriented channel geometries

ranging from narrow annuli to rectangular configurations. Operating pressures vary from atmospheric to highly pressurised conditions (up to 138 bar), with mass fluxes spanning over an order of magnitude (150–7700 kg/m^{2}s). Subcooling values range between 0 and 109 K, and contact angles are drawn from either reported measurements or representative literature values. This diversity ensures that the assessments cover conditions representative of both laboratory-scale studies and reactor-relevant flows. The aggregate dataset consists of 127 individual test cases and over 1,100 data points. Fig. 4 shows the boiling curves from each dataset. Fig. 3 further visualises the spread of flow parameters and material properties, demonstrating the variability in the database. A statistical summary of the flow conditions is given in Table 4.

Table 2: Summary of experimental datasets and test conditions for the flow boiling cases. n cases represents the number of boiling curves, while n points represents all the data points in all the boiling curves.

Dataset	Fluid	Channel	Surface	G (kg/m^{2}s)	u (m/s)	ΔT_{sub} (K)	P (bar)	θ (°)	D_h (mm)	n cases	n points
Phillips [52]	Water	Rect., Vertical	ITO	150 - 1250	0.16 - 1.30	5 - 155	1.01 - 2.0	86.5	16	54	502
Richenderfer et al. [18, 53]	Water	Rect., Vertical	ITO	500 - 2000	0.52 - 2.09	5 - 20	1.01 - 5	86.5	15	30	370
Chen et al. [54]	Water	Ann., Vertical	Stainless steel	200	0.2	40	1.01	90	19.1	1	6
Kennel [55]	Water	Ann., Vertical	Stainless steel		0.30 - 3.66	11.1 - 83.3	2 - 6	55	18.5, 10.6	13	100
Lee et al. [56]	Water	Ann., Vertical	Zircaloy-4	750	1.0	76	1	81.35	10.5	1	17
Seong et al. [57]	Water	Rect., Vertical	Zircaloy-4	1000	1.0	10	1.01	43	10	1	31
Morozov [58]	Water	Ann., Vertical	Stainless steel	795, 819	1.0	0	31, 40.8	38 [59]	3.2	2	11
Rohsenow & Clark [60]	Water	Ann., Vertical	Nickel	2660 - 7730	3.05 - 9.14	69.5 - 109.0	103.4, 137.9	38 [59]	4.6	5	30
Lie et al. [61]	R-134a	Ann., Horizontal	Copper	200 - 300	8.43 - 12.64	6, 13	4.88	6.5 [62]	2, 4	5	50

Table 3: Summary of experimental datasets and test conditions for the pool boiling cases.

Dataset	Fluid	Surface	P (bar)	θ (°)	n cases	n points
Gerardi et al. [63]	Water	ITO	1.01	80	1	6
Kim & Kim [26]	Water	SiO2	1.01	44	1	12
Kim et al. [64]	Water	Copper	1.01	60	1	17
Chang & Ferng [65]	Water	Copper	1.01	60	1	18
Benjamin & Balakrishnan [66]	Water	Aluminium	1.01	70	1	8
Kurihara & Myers [67]	Water	Copper	1.01	60	1	13

Table 4: Statistical summary of flow conditions across all the flow boiling data.

Parameter	Minimum	Maximum	Mean	Mode
Mass flux [kg/m^{2}s]	150	7729	1132	1000
Velocity [m/s]	0.16	12.6	1.62	1.22
Pressure [bar]	1.0	137.9	8.3	2.0
Subcooling [K]	0	109.0	17.9	10.0

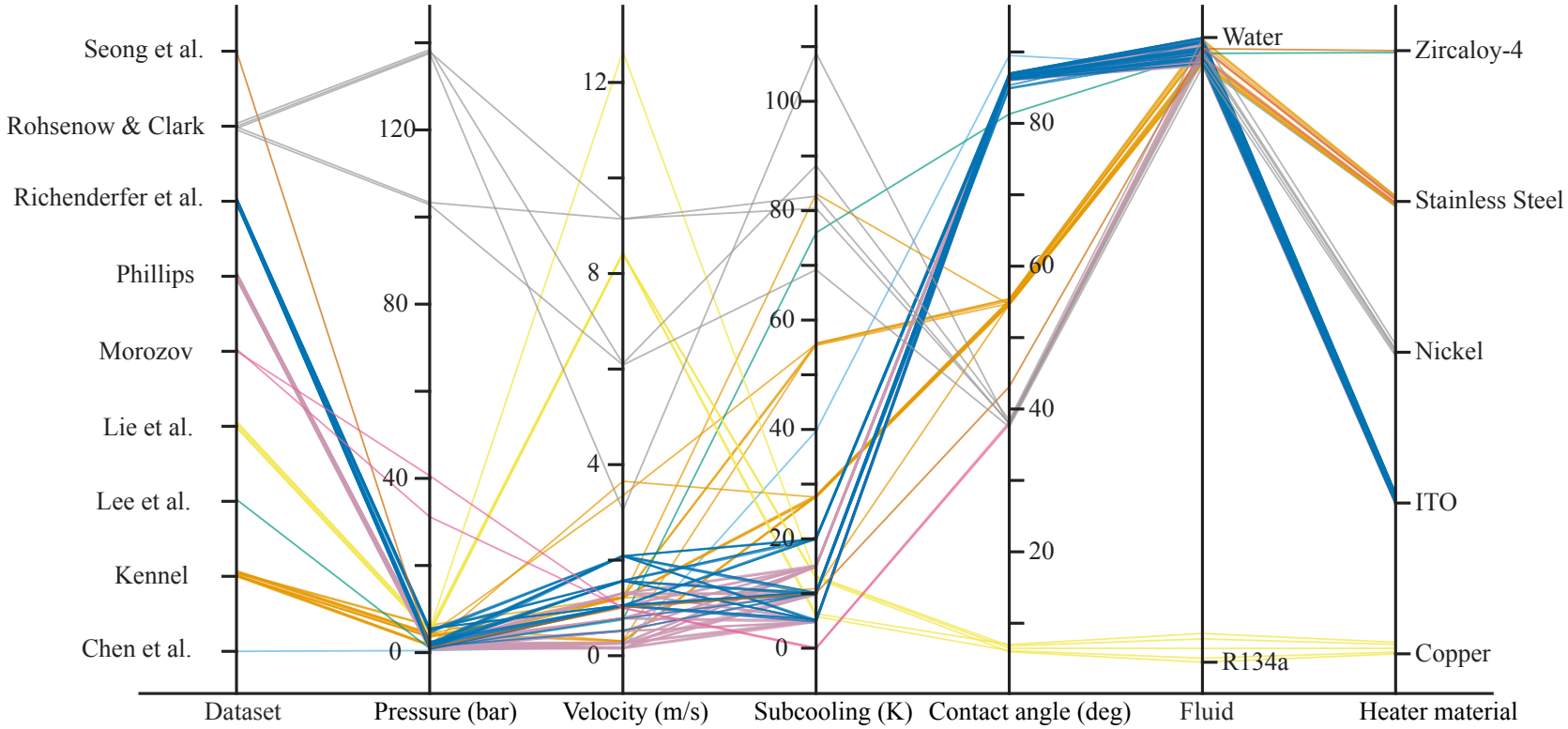

Figure 3: Flow boiling datasets in Table 2 visualised as a parallel plot illustrating the spread and variability of key parameters.

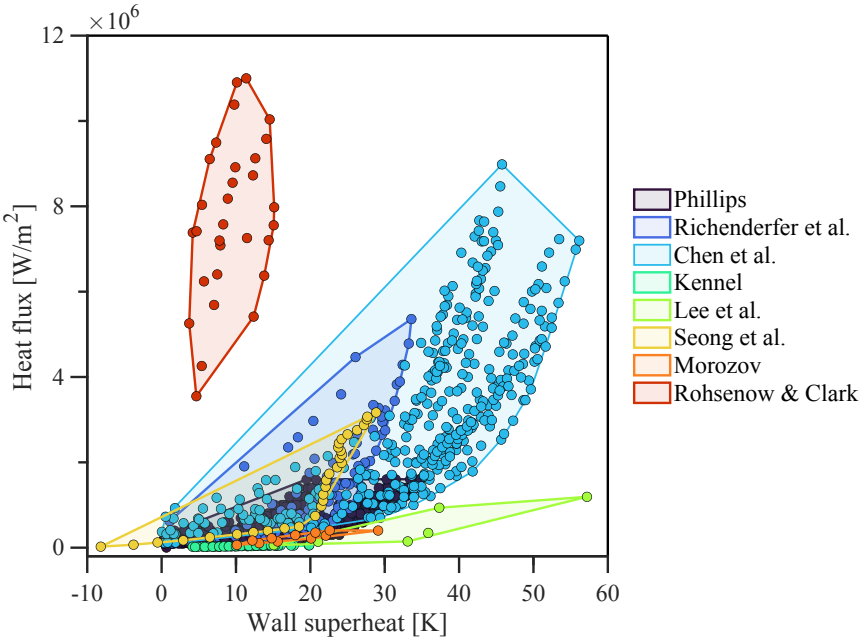

Figure 4: Boiling curves for flow boiling data selected for the assessments. Each shaded region represents a different datasets shown in Table 2.

The pool boiling database (Table 3) complements the flow data by including six independent datasets, all conducted under atmospheric pressure but on surfaces with different materials and wettability (ITO, SiO_2, copper, aluminium).

3.2. Evaluation methodology

The modelling framework described in Section 2 allows for a large number of possible configurations, arising from the combination of the heat flux partitioning formulations with the many available sub-models for bubble dynamics parameters. Assessing the predictive capability of such a large model space requires a systematic strategy. To this end, we have a two-level evaluation approach: the best case configuration (HFP and bubble parameter sub-models), and the best overall configuration.

- **Best case configuration**: represents the configuration that achieves the lowest prediction error for a given boiling curve. Since it tests whether the available boiling models are capable of reproducing the experimental measurements for a specific boiling curve (i.e. a very narrowly defined flow condition) it reflects the upper bound of performance achievable with the tested boiling models.

- **Best overall configuration**: represents the configuration that achieves the lowest aggregate error across all boiling curves in the database. It tests the generalisability of the various tested configurations. To identify the best overall configuration, the top-performing configurations from each case are pooled together and re-evaluated (one-at-a-time) across the entire dataset. The configuration with the smallest average error is then selected as the best overall.

Model accuracy is quantified using two complementary error metrics. The mean-squared error (MSE),

$$\mathrm{MSE} = \frac{1}{N}\sum_{i=1}^{N}\left(q_i^{\mathrm{pred}} - q_i^{\mathrm{exp}}\right)^2,$$

where q_i^{pred} and q_i^{exp} are the predicted and experimental heat fluxes at a given wall superheat, and N is the number of points in the boiling curve. MSE penalises large deviations more strongly and is used as the primary criterion to rank configurations and to identify the best case and best overall models. The second metric is the mean absolute percentage error (MAPE),

$$\mathrm{MAPE} = \frac{100}{N}\sum_{i=1}^{N}\left|\frac{q_i^{\mathrm{pred}} - q_i^{\mathrm{exp}}}{q_i^{\mathrm{exp}}}\right|,$$

which provides a normalised measure of relative error. MAPE facilitates comparisons across datasets with different magnitudes of heat flux and is particularly useful for summarising performance trends over multiple experimental conditions.

4. Results and discussions

4.1. Flow boiling model prediction assessment

Fig. 5 shows predicted boiling curves for four representative flow boiling conditions, alongside experimental measurements. For each case, the shaded regions represent the envelope of predictions from the top-n (with $n_{\max} = 2000$) configurations ranked by error, illustrating the variability introduced by different combinations of bubble parameter sub-models. The best-performing configuration with each HFP model for each test case is shown explicitly, along with the best overall configuration identified through the method discussed in Section 3.2. The best configuration for each case and the best overall configuration across all the cases are summarised in Table 5. The curves demonstrate that the HFP models are capable of reproducing the general shape of the boiling curve when paired with appropriate sub-models for

bubble parameters. However, the best overall model exhibits consistently higher errors across all cases, highlighting the limitations of a single global configuration in capturing the full variability of flow boiling conditions, especially when the pressure and subcooling are high (see Fig. 5 (b) and (d)).

Table 5: The best-case configurations for the four flow boiling conditions shown in Figure 5, along with the best overall configuration used across all cases. Each column corresponds to a case from subfigures (a)–(d), as indicated in the header.

Model	(a) $p = 1$ bar $\Delta T_{\text{sub}} = 10$ K $u = 1$ m/s	(b) $p = 6$ bar $\Delta T_{\text{sub}} = 28$ K $u = 1$ m/s	(c) $p = 31$ bar $\Delta T_{\text{sub}} = 0$ K $u = 1$ m/s	(d) $p = 138$ bar $\Delta T_{\text{sub}} = 80$ K $u = 9$ m/s	Best Overall
HFP	RPI	MIT	MIT	MIT	MIT
BDD	Fritz	Tolubinsky & Kostanchuk	Van Stralen & Zijl	Tolubinsky & Kostanchuk	Van Stralen & Zijl
BDF	Peebles & Garber	Cole	Stephan	Stephan	Stephan
NSD	Li et al.	HI-MIT	Lemmert & Chawla	Yang et al.	Lemmert & Chawla
BGT	Van Stralen et al.	MIT	Lee et al.	Van Stralen et al.	Lee et al.
BWT	MIT	MIT	MIT	Van Stralen et al.	Van Stralen et al.
CHT	Churchill & Chu	Churchill & Chu	Gnielinski	Churchill & Chu	Gnielinski

Figure 6 compares the predicted bubble parameters and the total heat flux for the top 200 configurations ranked by MSE against experimental boiling curve data for the Richenderfer et al. [18] case at $p = 1.01$ bar, $u = 1.04$ m/s, and $\Delta T_{\text{sub}} = 10$ K. This dataset also provides measurements of the bubble parameters which allows further assessment of the various models. Despite all configurations exhibiting close agreement with the experimental heat flux (top-left panel), the predicted values for individual bubble parameters (departure diameter, frequency, nucleation site density, growth time, and wait time) span several orders of magnitude across the model configurations. This discrepancy highlights how, sometimes, good accuracy is only the result of the compensatory nature of errors among sub-models: inaccuracies in one bubble parameter (e.g., an over-prediction of site density) may be offset by deviations in others (e.g., under-prediction of growth time), resulting in heat flux predictions that remain quantitatively accurate. Notably, even the best-case and best-overall configurations, while matching the total heat flux well, show visible deviation from the experimental trends in most bubble parameter plots. The largest variability in predictions with different models is observed for the bubble departure frequency, wait time, and the nucleation site density. All the models over-predict the nucleation site density by orders of magnitude. These suggest that the various sub-models are not able to capture the underlying physical boiling phenomena and thus struggle to generalise, as demonstrated in discussions thus far.

Fig. 7 compares predicted and experimental heat fluxes across all datasets using the best overall configuration for each of the three heat flux partitioning models,

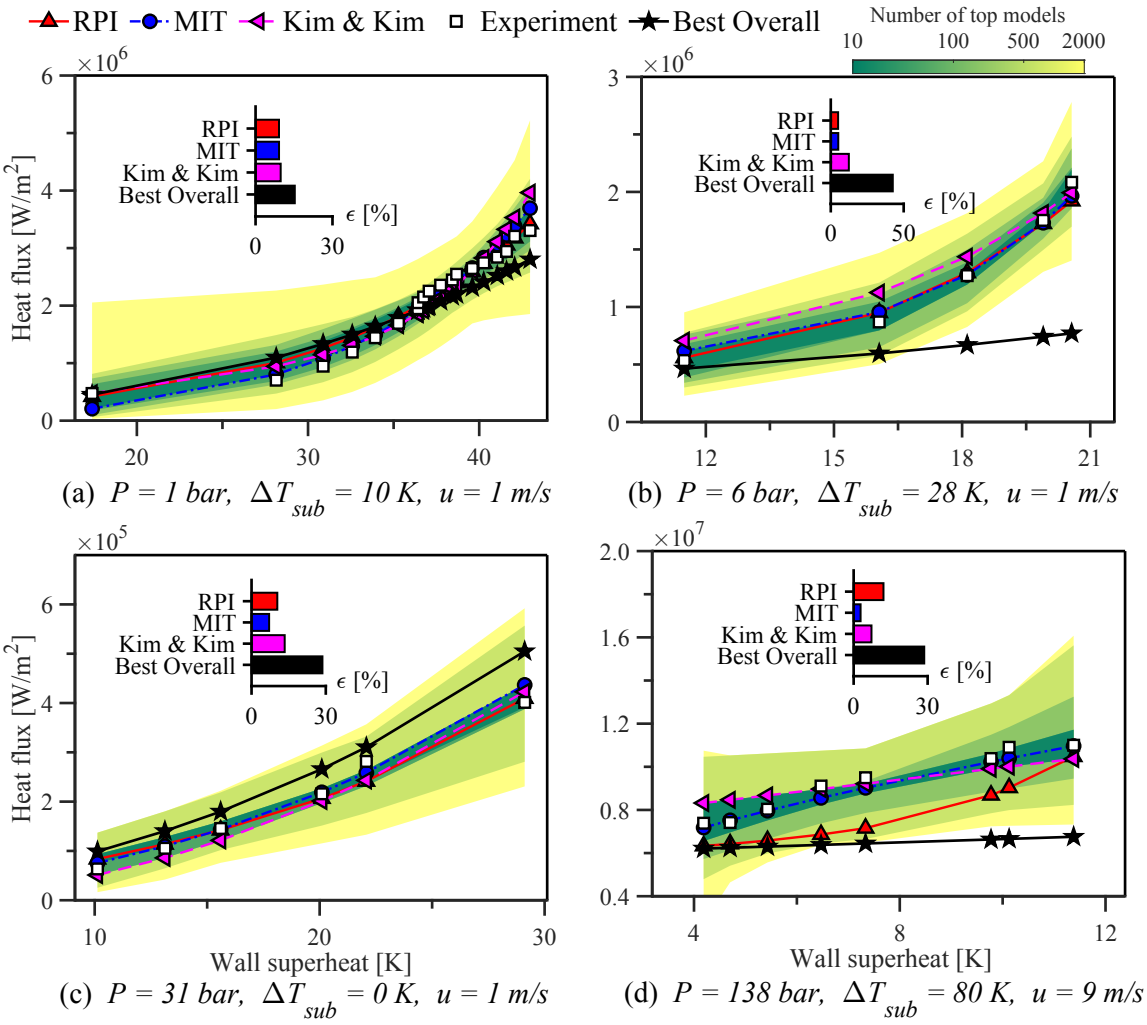

Figure 5: Sample boiling curves for different flow conditions. Shaded regions indicate the envelope formed by the minimum and maximum predictions among the top-n model configurations, ranked by agreement with experimental data. For each case, the best-performing prediction from the HFP models—RPI, MIT, and Kim & Kim—is also shown for comparison. The bar charts show the mean-absolute percentage error relative to the experimental measurements.

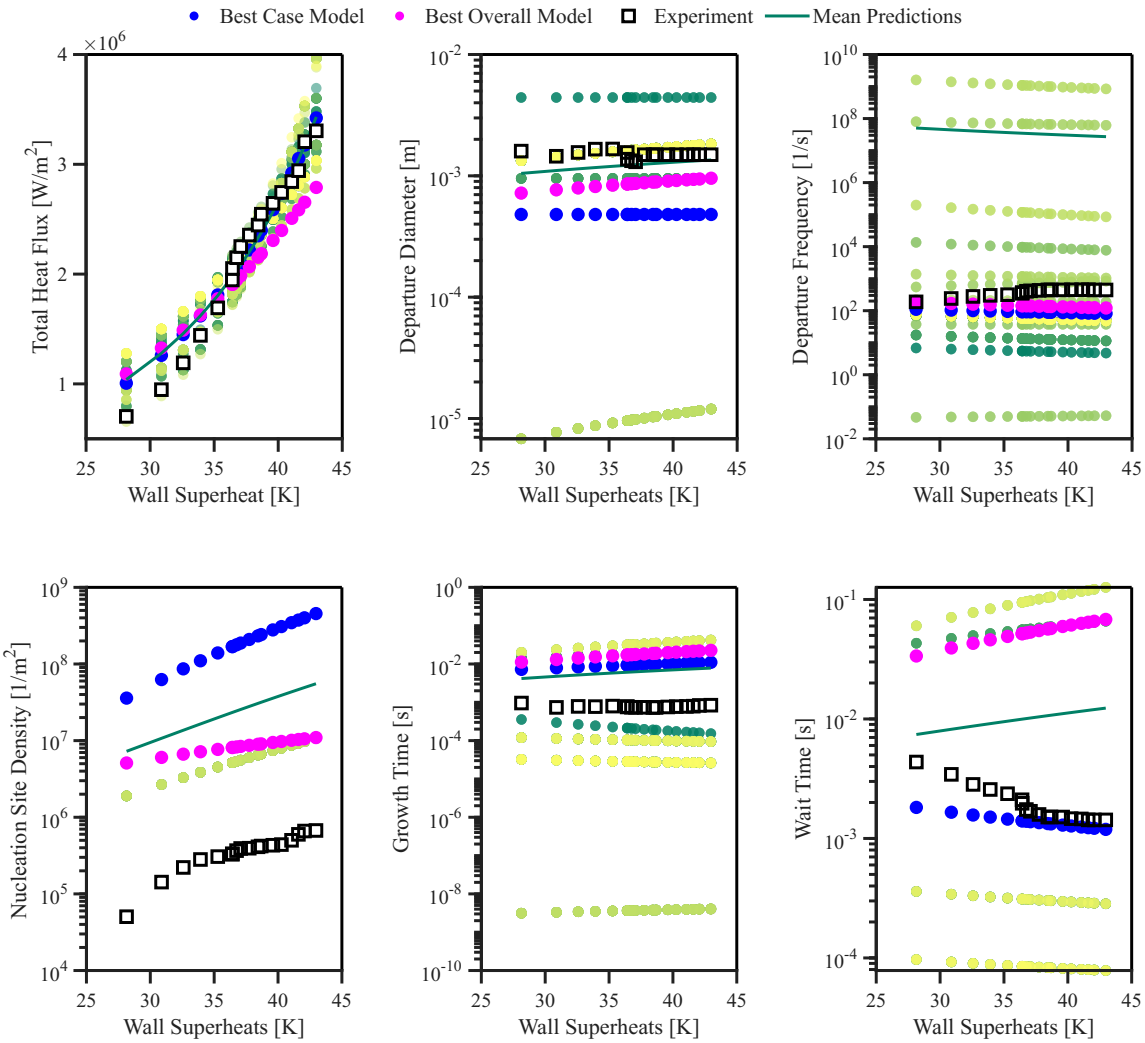

Figure 6: Comparison of the predicted and experimental total heat flux and individual bubble parameters for Richenderfer et al. [18] at $p = 1.01$ bar, $u = 1.04$ m/s, and $\Delta T_{\text{sub}} = 10.0$ K. The top 200 models are shown as green scatters.

as well as the combination of all the best-performing configuration for each case. The shaded region denotes predictions within ±50% of the experimental values. As expected, the best-per-case configuration (subplot d) yields the highest accuracy, while there are significant discrepancies for the fixed configurations for each of the three heat flux partitioning models (subplot (a) - (c)). These configurations, which show the least average MSE for each HFP across all the data, are shown in Table 6. The fraction of predictions falling within ±50% of the experimental heat fluxes

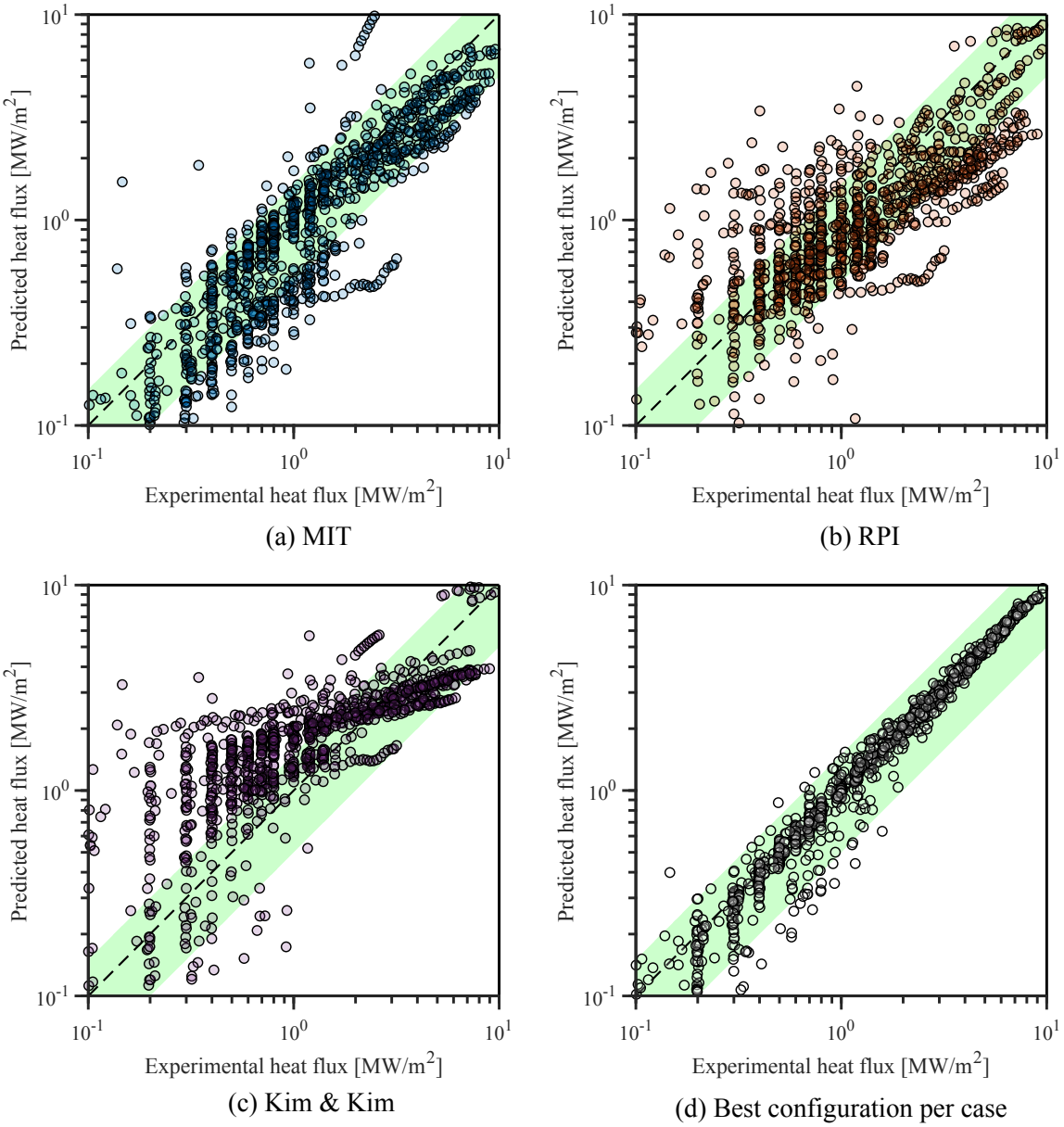

Figure 7: Predicted vs. experimental heat fluxes for the three heat flux partitioning models. Shaded green region illustrates predictions within $\pm 50\%$ of the experimental values. Subplots (a) to (c) show the configurations with the lowest global error (averaged across all datasets) for each HFP model. Subplot (d) combines all the configurations with the minimum error for each case.

varies noticeably across models: 70% for MIT, 59% for RPI, and only 45% for Kim & Kim, highlighting the challenges of predicting all flow and operating conditions with a single formulation.

Table 6: Best overall configurations for each HFP model based on lowest average MSE for the all the data, along with the fraction of predictions within ±50% of experimental heat fluxes (see Figure 7).

Bubble Parameter	Heat flux partitioning model		
	MIT	RPI	Kim & Kim
Departure diameter	Van Stralen & Zijl	MIT	Cole
Departure frequency	Stephan	Exact	Zuber
Nucleation site density	Lemmert & Chawla	Yang et al.	Hibiki & Ishii MIT
Growth time	Lee et al.	Lee et al.	Van Stralen et al.
Wait time	-	MIT	Van Stralen et al.
Convective heat transfer	Gnielinski	Churchill & Chu	Churchill & Chu
Fraction within ±50%	0.70	0.59	0.45

In contrast to overall errors, Table 7 provides a detailed breakdown of prediction errors across individual flow boiling datasets for each of the heat flux partitioning model configurations. The MIT formulation achieves the lowest error for six of the nine datasets, indicating a better generalisability across a broad range of boiling conditions compared to the other two HFP models. RPI performs best for three datasets, while the Kim & Kim model does not outperform the others on any dataset.

To understand these differences, it is instructive to examine the characteristics of each dataset (summarised in Table 2) and the associated sub-model combinations (see Table 6). For datasets such as Kennel, Phillips, Richenderfer et al., and Morozov, the MIT configuration consistently yields the lowest errors. These datasets span a wide range of pressures (from 1 to 31 bar), flow velocities, and subcooling values. Additionally, the MIT model has been partially developed and validated against data from Richenderfer et al. [18] and Phillips [52] and it is therefore expected to perform well under these conditions. Compared to the other configurations, this model combination performs better across a wider range of flow conditions. In contrast, the RPI model shows competitive or superior performance for the datasets of Chen et al., Lee et al., and Lie et al.. For example, Lie et al. features R-134a refrigerant in a horizontal channel configuration–significantly different from the water-based, vertically orientated flows in other datasets. The other two configurations show a very large error for this dataset which highlights the sensitivity of the sub-models to the flow orientation and working fluid. The Kim & Kim model consistently yields the

highest errors, with MAPE values exceeding 1000% in some cases (see, e.g., Lie et al.). This can be attributed to the original development of the model for pool boiling scenarios, which are less suited to the forced convection environments present in these datasets.

Table 7: Comparison of average mean-squared error and the average mean-absolute percentage error (MAPE) for each dataset and HFP model. Lowest errors for each dataset is underlined.

Dataset	MSE $\times 10^{12}$ [W^2/m^4]			MAPE [%]		
	RPI	MIT	Kim & Kim	RPI	MIT	Kim & Kim
Chen et al.	<u>2.29</u>	4.48	8.92	453.1	<u>442.0</u>	1263.9
Kennel	0.99	<u>0.63</u>	1.55	97.5	<u>28.8</u>	188.7
Lee et al.	<u>0.26</u>	31.26	7.05	<u>35.4</u>	235.1	141.4
Lie et al.	<u>0.00</u>	0.18	6.79	<u>52.0</u>	1096.7	6939.7
Phillips	0.13	<u>0.08</u>	0.46	47.5	<u>34.2</u>	117.7
Seong et al.	2.17	2.26	<u>0.67</u>	61.6	64.7	<u>50.0</u>
Morozov	1.43	<u>0.00</u>	2.49	330.6	<u>26.4</u>	727.0
Rohsenow & Clark	<u>3.07</u>	7.01	10.94	<u>21.9</u>	30.5	44.9
Richenderfer et al.	0.47	<u>0.09</u>	0.32	25.8	<u>16.0</u>	43.5

While the previous discussions have focused on a small number of specific configurations—such as best overall or best-case models—these only represent a narrow slice of the broader model space. In contrast, Table 8 provides a more comprehensive view by reporting the frequency with which individual sub-models appear within the top 100 configurations for each case, ranked by accuracy (based on MAPE).

Among HFP formulations, the RPI model appears most frequently, followed by Kim and Kim and MIT. This result contrasts with the best overall models discussed thus far, and shown in Table 6, where MIT had the lowest average error across most datasets. However, a key limitation of this frequency-based analysis is that it treats each sub-model independently, without accounting for interdependencies between model components. As demonstrated in previous sections, it is the full configuration—the specific combination of heat flux partitioning model and bubble parameter sub-models—that determines prediction accuracy. Simply counting the frequency of individual models may obscure the importance of these interactions. For example, the configuration shown in Table 6, which combines the MIT HFP formulation with carefully selected bubble departure, frequency, site density, and convection models, consistently yields the most accurate predictions across the full dataset. This underscores that performance is not solely a function of individual model quality, but of synergistic effects across the model chain, including compensatory effects of errors from the various sub-models. However, this aggregated frequency analysis can still

offer an insight into which models are consistently associated with high-performing predictions and which are less commonly selected (this may highlight the lack of robustness of some sub-models).

Table 8: Frequency of individual sub-models across all datasets and cases. For each case, the top 100 configurations (based on average prediction error using MAPE) were identified, and the occurrence of each sub-model was counted across these top-performing configurations. Frequencies are reported as percentages of total appearances within the top 100 sets.

Category	Model	Freq.	Category	Model	Freq.
HFP	RPI	42.1%	**Convective**	Gnielinski	68.9%
	Kim & Kim	30.0%		Churchill & Chu	31.1%
	MIT	27.9%			
Departure Diameter	Phan et al.	19.3%	**Departure Freq.**	Zuber	21.3%
	Tolubinsky & Kostanchuk	17.2%		Stephan	20.1%
	Golorin & Kolchugin	12.5%		Peebles & Garber	16.5%
	MIT	12.4%		Sakashita & Ono	15.8%
	VanStralen & Zijl	9.3%		Cole	15.6%
	Colombo & Fairweather	8.2%		Exact	10.7%
	Ruckenstein	5.5%			
	Cole	5.3%			
	Kocamustafaogullari	3.1%			
	Bovard et al.	2.7%			
	Fritz	2.6%			
	Nam et al.	1.9%			
Nucleation Site Density	Li et al.	22.6%	**Growth Time**	Lee et al.	38.6%
	Yang et al.	20.8%		MIT	31.2%
	Lemmert & Chawla	20.5%		Van Stralen et al.	30.2%
	Hibiki & Ishii MIT	14.1%	**Wait Time**	MIT	51.9%
	Hibiki & Ishii	13.1%		Van Stralen et al.	48.1%
	Wang & Dhir	8.9%			

In terms of bubble departure diameter, no single model dominates, although the models of Phan et al. and Tolubinsky & Kostanchuk are the most frequent. Interestingly, the widely used Van Stralen & Zijl and Fritz models appear less often, although this may be again due to the aforementioned limitation of the frequency-based analysis not accounting for model interdependencies. For departure frequency, Zuber's model is the most common, closely followed by the Stephan model. The Peebles & Garber, Sakashita & Ono and Cole models perform similarly. This distribution highlights the absence of a universally optimal frequency model and suggests that multiple formulations offer competitive performance depending on the scenario. In the nucleation site density category, Li et al. and Yang et al. are the most frequent, followed closely by Lemmert & Chawla. It is interesting to note that these prominent models are much simpler than alternative Hibiki-Ishii (HI) and the MIT-modified HI models. This may mean that the simpler models may be more robust. Additionally,

the most frequent nucleation site density model, i.e. the Li et al. model, explicitly incorporates pressure as a parameter in its formulation, which may contribute to its robust performance across datasets spanning a wide pressure range. Finally, for convective heat transfer (CHT), Gnielinski appears most prominently, which may highlight the advantage of using Reynolds- and Prandtl-number-sensitive formulations in forced convection subcooled boiling conditions.

4.2. Sensitivity analyses for flow boiling cases

4.2.1. Flow conditions

To explore the influence of flow conditions (Table 2) on prediction accuracy (Table 7), Figure 8 presents the distribution of mean-absolute percentage error across all cases as a function of pressure (Fig. 8a) and subcooling (Fig. 8b). The sensitivity to velocity changes has not been considered due to the limited number of cases at each distinct velocity in the database. Each boxplot represents the MAPE distribution for all cases at a given pressure or subcooling level using the best overall configuration, shown in Table 5. The results show that prediction error does not vary monotonically with either pressure or subcooling.

While slightly lower MAPE values are observed for pressures around 1–1.5 bar and moderate subcooling levels (10–20 K), the spread of errors remains wide across most bins. At higher pressures, such as 31 and 138 bar, error values are consistently high but sparse, reflecting the limited number of cases at these conditions. Overall, the error tends to increase at higher pressure values (i.e. $P > 2$ bar), while there does not seem to be any strong or consistent trend when the subcooling values change. It must be noted that the analysis is based on a single best overall configuration. The absence of clear trends in these results does not rule out pressure or subcooling effects in other model configurations.

Since the previous discussion focused on a single best overall configuration, it is also valuable to examine whether certain model combinations perform consistently better within specific pressure ranges. This is motivated by the fact that key boiling phenomena (such as nucleation, microlayer formation, and bubble growth) are strongly pressure-dependent, and some sub-models explicitly include pressure in their formulation. To explore this, the full pool of model configurations was filtered to include only those ranked in the top 10 per case, within three defined pressure bands: near atmospheric, intermediate ($1.2 < P \leq 6$ bar), and high pressure ($6 < P < 138$ bar). Each configuration in the pooled set was then re-evaluated across all cases in the corresponding pressure band using a mean-squared error criterion.

The results are shown in Figure 9 and Table 9. In each pressure band, the pressure-tuned configuration outperforms the global best configuration, achieving

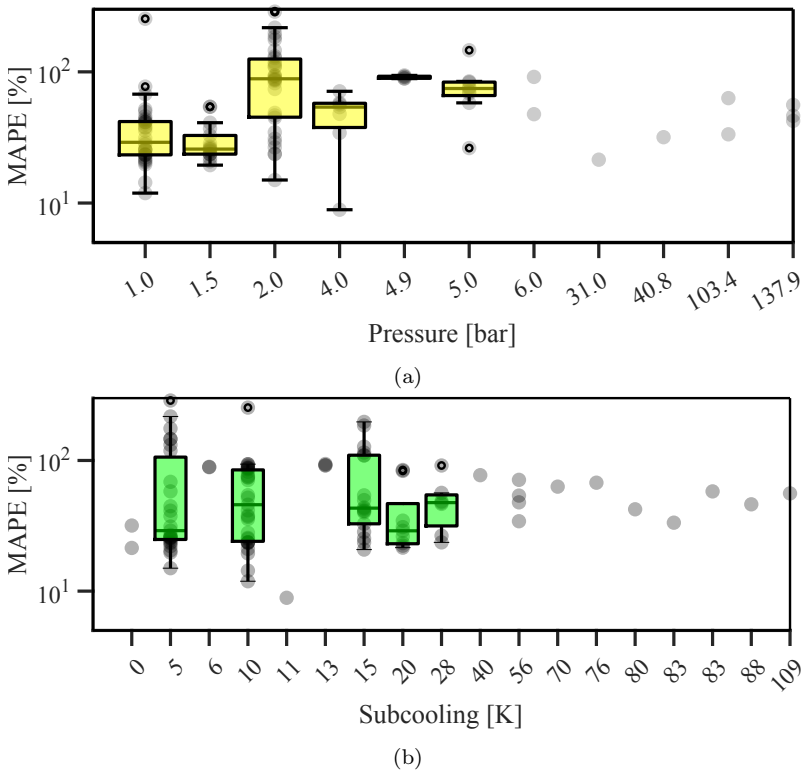

Figure 8: Mean-absolute percentage error of best-performing HFP configuration vs. pressure and subcooling.

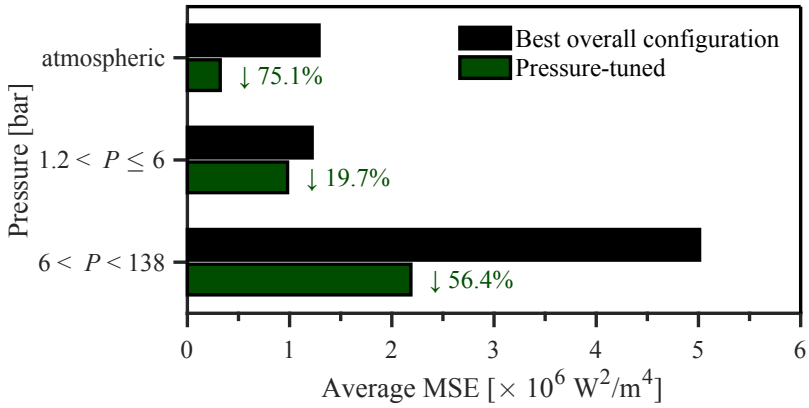

Figure 9: Comparison of prediction errors between the best overall configuration and pressure-tuned configurations.

Table 9: Best pressure-tuned model configurations for each pressure range.

Model	Pressure [bar]		
	Atmospheric	$1.2 < P \leq 6$	$6 < P < 138$
HFP	MIT	MIT	MIT
BDD	Tolubinsky & Kostanchuk	Tolubinsky & Kostanchuk	VanStralen & Zijl
BDF	Stephan	Stephan	Cole
NSD	Yang et al.	Yang et al.	Lemmert & Chawla
BGT	MIT	Van Stralen et al.	MIT
BWT	Van Stralen et al.	MIT	MIT
CHT	Gnielinski	Gnielinski	Churchill & Chu

reductions in average MSE of 75.1%, 19.7%, and 56.4% for the atmospheric, intermediate, and high pressure regimes, respectively. Notably, the MIT HFP model is selected in all three pressure bands, but the supporting sub-models vary with pressure. For instance, Tolubinsky & Kostanchuk is the preferred departure diameter model at low and intermediate pressures, while Van Stralen & Zijl performs best at high pressure. These trends suggest that while the same HFP formulation may be broadly effective, predictive accuracy still depends strongly on the choice of bubble dynamics sub-models and their interaction with operating conditions. This reinforces the idea that no single fixed configuration generalises optimally across all pressure ranges and highlights the potential need for targeted tuning of model configurations to specific pressure regimes.

The increased sensitivity observed under high pressure can be interpreted as an amplification of modelling inaccuracies, and regime-dependent changes in bubble dynamics. Many bubble parameter correlations/models and heat flux partitioning formulations have historically been developed and validated using datasets obtained at atmospheric or moderately elevated pressures. Experimental measurements of bubble-scale quantities such as departure diameter, departure frequency, and nucleation site density are significantly more difficult to obtain at high pressure, and as a result most models/correlations are biased towards low pressure bubble dynamics. It has also been observed that at elevated pressures, bubbles typically detach at smaller diameters and higher frequencies, leading to increased nucleation activity and stronger dependence of the heat flux components on bubble-scale parameters [68]. In addition, microlayer evaporation, often considered a dominant contribution at lower pressures, becomes less pronounced as bubble size and microlayer lifetime decrease with increasing pressure, shifting the relative importance of the underlying heat transfer mechanisms [69]. These regime-dependent changes further explain the need for regime-tuned configurations.

4.2.2. Contact angle

The contact angle between the fluid and the heated surface plays a significant role in bubble dynamics, particularly in models for departure diameter, nucleation site density, and microlayer spreading. It is the tangential angle at the contact line between the base of a bubble and the wall. Despite its importance, the contact angle is not always measured in the experimental datasets considered in this study. When not available, a nominal value based on literature data is assumed, as tabulated in Tables 2 and 3. Additionally, it is argued that the contact angle is not static, but evolves as the bubble grows [70]. Given this uncertainty, it is important to assess how sensitive model predictions are to variations in contact angle. To this end, we perform a sensitivity analysis with the best overall configuration by perturbing the nominal values by ±20%.

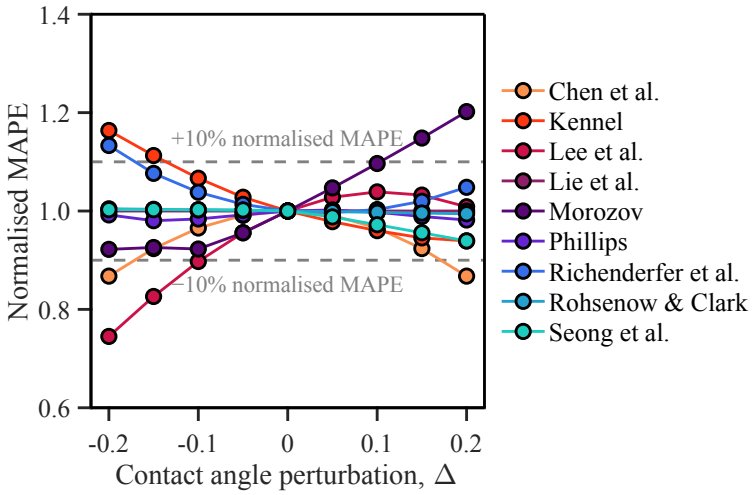

Figure 10: Sensitivity of the best overall configuration to the contact angle perturbations. Contact angle values are perturbed by ±20% of the nominal values used in Table 2. The normalised MAPE represents the average mean-absolute percentage error with the perturbed contact angle divided by the average MAPE using the nominal contact angle.

The results, shown in Figure 10, display the normalised mean-absolute percentage error as a function of perturbation level for each dataset. In general, moderate perturbations in the contact angle lead to relatively small changes in MAPE, with most datasets remaining within ±10% of the baseline error. This suggests that the best overall configuration is not highly sensitive to small inaccuracies in assumed contact angle values. However, some datasets show more pronounced variation. For example, the Lee et al. and Lie et al. datasets exhibit the highest sensitivity, with changes in MAPE exceeding 25% for a 20% perturbation. In contrast, the Richender-

fer et al. and Chen et al. datasets are among the least sensitive, showing very small changes across the full perturbation range. However, depending on the measurement uncertainties it can be seen that the contact angle can introduce errors in model predictions. It must be noted that these results apply specifically to the best overall configuration; other sub-model combinations may exhibit greater sensitivity to the contact angle depending on how strongly it influences their underlying formulations.

4.2.3. Sub-models

Thus far, we have conducted sensitivity analysis with respect to flow conditions (pressure and sub-cooling) and the contact angle. In this section, to better understand which aspects of the *modelling* framework most influence prediction accuracy, two complementary sensitivity analyses are conducted based on the best overall configuration identified for the flow boiling cases.

The first sensitivity analysis (Figure 11) adopts a parameter-level perspective, where individual bubble dynamics quantities, such as departure diameter, frequency, and growth time, are systematically perturbed using 1) a one-at-a-time approach, and 2) where all bubble parameters are simultaneously perturbed. We re-iterate, the analysis is based on the best overall configuration in Table 6. The analysis reveals substantial differences in how sensitive the model is to perturbations of various sub-models. In particular, the departure diameter model leads to significant variations in prediction error, followed by the nucleation site density, the departure frequency, and the single phase convection model (i.e. the Nusselt number correlation)–indicating strong dependence on these sub-models. In contrast, the bubble growth time model has a smaller influence. The results for the bubble wait time is shown for completeness, however it does not impact the best overall configuration, since there is no explicit use of a bubble wait time closure in the HFP formulation. The joint perturbation results in the highest average MAPE and widest error spread, highlighting strong interaction effects between bubble dynamics parameters.

An important feature visible in the perturbation results is the clear asymmetry in the error response: negative perturbations to bubble dynamics parameters consistently lead to larger increases in prediction error than positive perturbations of equal magnitude. This trend is most evident in the joint perturbation case but is also observed across individual parameters such as departure diameter, frequency, and nucleation site density. The asymmetry in error response arises from the nature of the MIT HFP model. Negative perturbations to bubble parameters significantly suppress the dominant evaporation contributions that are highly sensitive to parameters such as departure diameter, frequency, and nucleation site density. For instance, the microlayer term scales as $q''_{ml} \propto \rho_l h_{lv} f \overline{N_b} \delta_{ml} D^2_{ml}$, and the inception

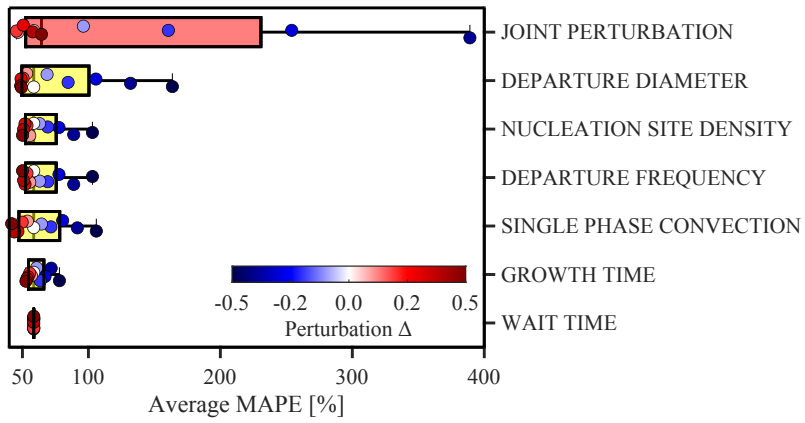

Figure 11: Sensitivity of bubble dynamic parameters evaluated by perturbing each parameter across a range of ±50% around their nominal value, while keeping the rest fixed. For each perturbation, the mean MAPE was computed across all cases. Box plots summarise the spread of average MAPE values for each sub-model category. Overlaid scatter points show individual perturbation results, coloured according to perturbation level.

term as $q''_{in} \propto \rho_v h_{lv} f \overline{N_b} D_{in}^3$. In both cases, f, $\overline{N_b}$, and D_d (which influences D_{ml} and D_{in}) appear multiplicatively and often with non-linear exponents. As a result, negative perturbations to any of these quantities sharply reduce the evaporation heat flux, leading to significant under-prediction of total heat transfer. In contrast, positive perturbations tend to saturate due to physical limits—for example, the sliding area factor S_{sl} is capped at unity—so further increases in f or $\overline{N_b}$ may yield only marginally higher heat fluxes.

The second analysis (Figure 12) instead explores sub-model-level sensitivity. Each sub-model used in the baseline configuration is individually substituted with alternative candidates from the full model library, while all other sub-models are held fixed. The mean-absolute percentage error is computed for each sub-model across all datasets, and the results are shown as box plots grouped by sub-model category. This allows for a direct comparison of competing sub-models within each category (e.g., bubble departure diameter or convective heat transfer), providing insight into which closures tend to generalise better when embedded within a high-performing configuration.

The results reveal that sub-model choices for bubble departure diameter and nucleation site density have the largest influence on model accuracy. Within the BDD category, models such as Tolubinsky & Kostanchuk and Van Stralen & Zijl produce the lowest MAPE values and relatively narrow error distributions, suggesting robust performance. In contrast, models like Ruckenstein and Kocamustafaogullari

exhibit both high error and large variability, indicating poor generalisability. A similar trend is observed in the NSD category, where simpler correlations (e.g., Yang et al., Lemmert & Chawla) consistently outperform more complex alternatives such as the HI-MIT model. Other sub-model categories exhibit less pronounced but still meaningful variation. For departure frequency, Zuber and Stephan show strong performance, while Peebles & Garber and MIT are more variable. In growth time, all models exhibit comparable accuracy, but the MIT formulation yields the narrowest spread. For convective heat transfer, Gnielinski emerges as the most consistent performer, likely due to its inclusion of Reynolds and Prandtl number effects.

The combined results from both perturbation-based and sub-model substitution analyses consistently point to bubble departure diameter, nucleation site density, and bubble departure frequency as the most influential parameters. These components not only showed the largest impact on prediction error when perturbed numerically, but also exhibited the widest spread in accuracy when alternative sub-models were substituted. This reinforces their critical role in determining heat flux predictions and highlights the need for improved physical modelling for these models.

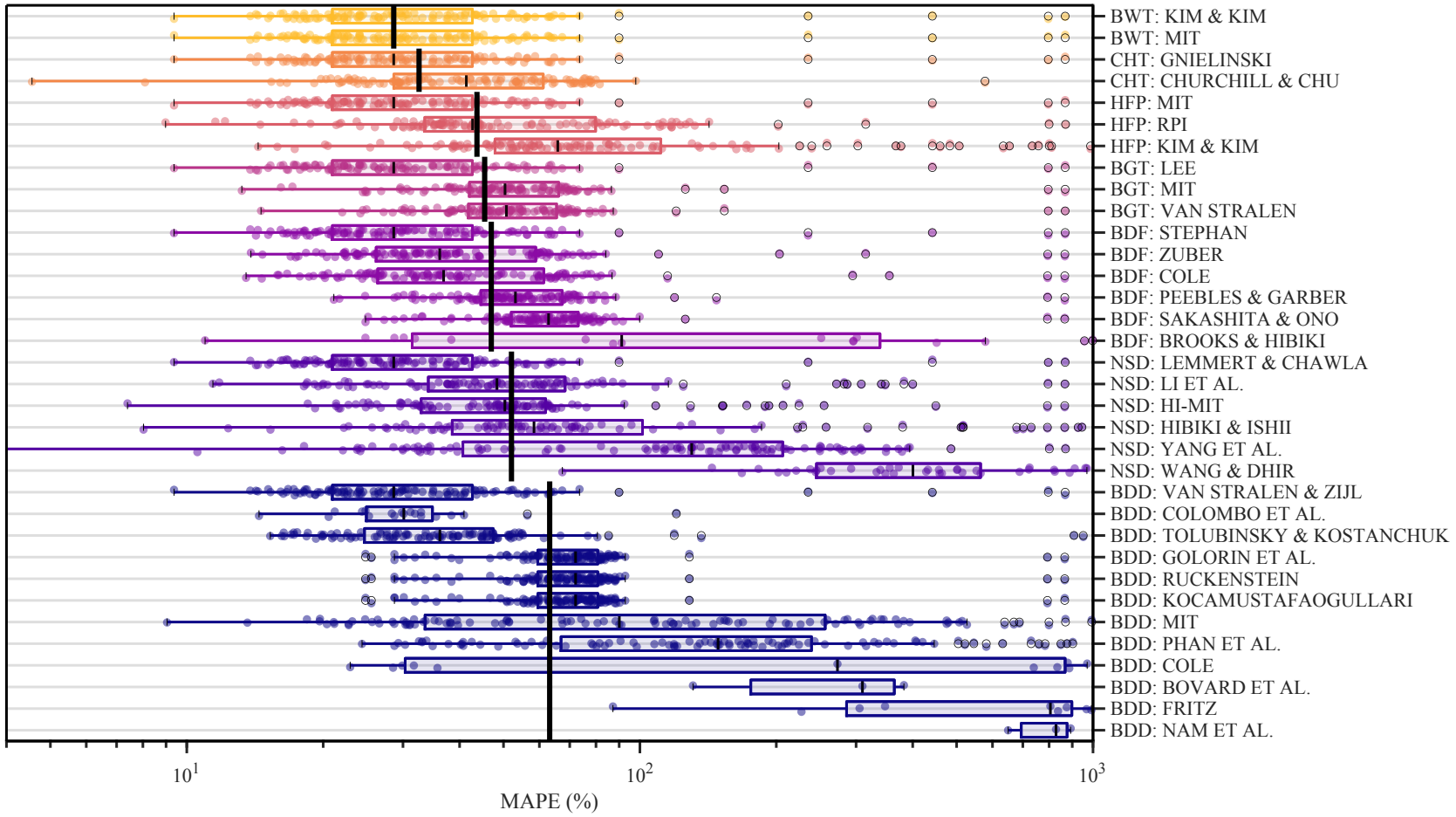

Figure 12: Sensitivity analysis of all the sub-models. Each sub-model shown corresponds to a modification of the baseline configuration (based on the best overall configuration) by replacing a single sub-model while holding all others fixed. The distribution of mean-absolute percentage error is computed per case (shown as scatter points) across all the dataset. Box plots and overlaid scatter points indicate the variation in prediction accuracy for each sub-model choice. Sub-models are grouped and colour-coded by category. Solid black lines indicate the median MAPE across all sub-models within each category.

4.3. Pool boiling

To complement the findings from the flow boiling analysis, a subset of representative results is also presented for pool boiling conditions. These include sample boiling curves, a comparison of predicted versus experimental heat fluxes across all datasets, and per-case best configurations. For brevity, only a limited selection of results is shown; however, they are representative of broader trends observed across the full pool boiling dataset.

Figure 13 compares predicted and experimental heat fluxes using the best overall configuration and best-per-case models. As in the flow boiling analysis, the predictions from a single global model are significantly outperformed by configurations tuned for individual cases. This reinforces the key insight that no universal model can accurately reproduce boiling behaviour across all conditions.

Table 10: Best overall configuration for the pool boiling cases.

HFP	BDD	BDF	NSD	BGT	BWT	CHT
RPI	Van Stralen & Zijl	Zuber	Lemmert & Chawla	Lee et al.	Van Stralen et al.	Churchill & Chu

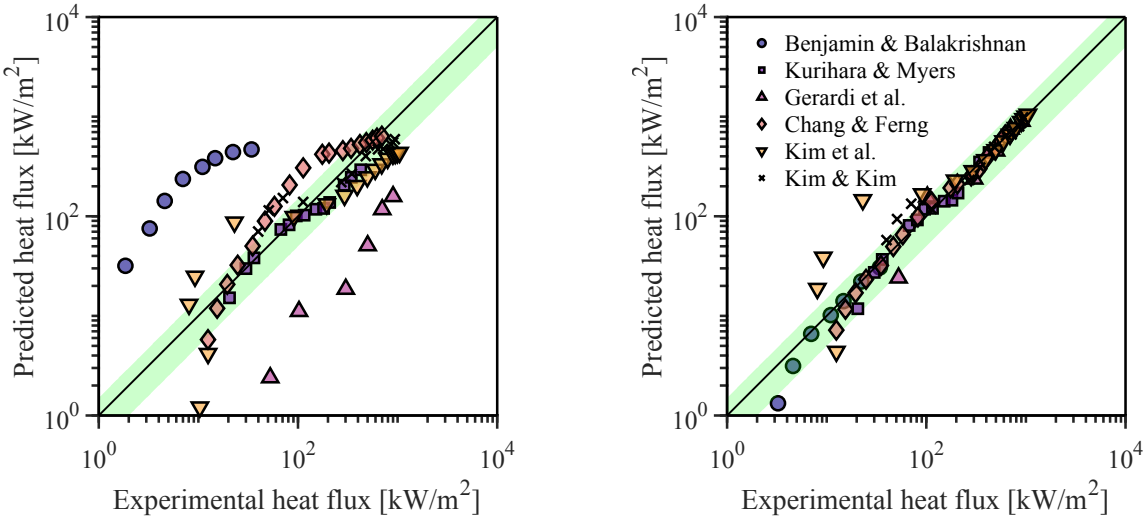

(a) Best overall model configuration

(b) Best model for each case

Figure 13: Comparison between the best overall configuration and per-case best configuration in predicting heat flux in pool boiling. The green band represents ±50% deviations.

Sample boiling curves for three pool boiling cases are shown in Figure 14. The shaded regions again illustrate the envelope of predictions from the top-n configu-

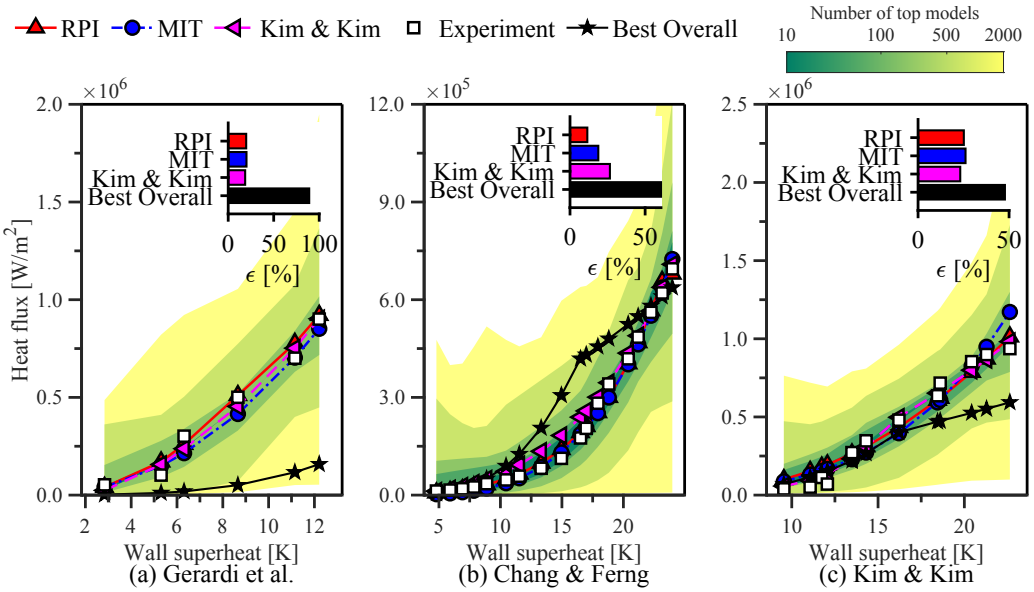

Figure 14: Sample boiling curves for pool boiling datasets.

rations, while explicit comparisons are made with the best-performing HFP models. Consistent with earlier observations, accurate total heat flux predictions can be achieved when the 'right' combination of sub-models are used. However, the best overall configuration can be significantly inaccurate, e.g. the Gerardi et al. case in Fig. 14(a). The performance of the three heat flux partitioning (HFP) models

Table 11: Performance of each HFP model using MSE and MAPE across pool boiling datasets.

Dataset	MSE [$\times 10^6$ W^2/m^4]			MAPE [%]		
	RPI	MIT	Kim & Kim	RPI	MIT	Kim & Kim
Kurihara & Myers	<u>0.00</u>	0.01	29.68	<u>18.3</u>	31.2	2610.3
Kim & Kim	0.04	0.15	<u>0.00</u>	47.7	67.7	<u>25.6</u>
Kim et al.	<u>0.10</u>	0.16	82.04	<u>72.1</u>	89.2	2685.0
Gerardi et al.	0.20	0.10	<u>0.03</u>	89.0	131.2	<u>50.7</u>
Chang & Ferng	0.01	<u>0.00</u>	253.58	60.6	<u>24.5</u>	5563.2
Benjamin & Balakrishnan	0.08	<u>0.05</u>	48.46	2318.3	<u>2021.6</u>	56803.5

is summarised in Table 11, which shows both MSE and MAPE for each dataset. Similar to the flow boiling cases, the predictive accuracy depends strongly on both the selected HFP formulation and the accompanying bubble dynamics sub-models.

Notably, the Kim & Kim HFP model performs well on the Kim & Kim and Gerardi et al. datasets, precisely the data against which the model was originally validated. For other cases, however, its performance is significantly weaker.

Overall, the conclusions drawn from the pool boiling analysis mirror those of the flow boiling cases: accurate predictions require careful selection and tuning of both HFP and bubble dynamics models, and there is no single configuration that universally outperforms across all pool boiling datasets.

4.4. Comparison of HFP models with experimental bubble parameters

The preceding analyses evaluated the heat flux partitioning models in conjunction with various sub-models to predict bubble dynamics parameters. However, the predictive performance of HFP models is inherently coupled with the accuracy of these sub-models, making it difficult to isolate the capabilities of the HFP formulation on its own. To address this, we again take advantage of the Richenderfer et al. [18] dataset, which provides experimentally measured bubble parameters across multiple mass fluxes, atmospheric pressure, and subcooling of 10 K. These include direct measurements or estimates of departure diameter, frequency, growth time, wait time, and nucleation site density.

In this section, we assess the predictive accuracy of the HFP models by directly supplying them with the experimental bubble parameters, thereby removing the uncertainties associated with sub-model closures. This enables a focused evaluation of the HFP formulations. Only the MIT and RPI models are considered in this analysis, as earlier results have shown that the Kim & Kim model (developed for pool boiling) consistently underperforms in forced convection flow boiling scenarios. Since single-phase heat transfer coefficient measurements are not provided in the datasets, we use the Gnielinski Nusselt number correlation in both HFP models, based on the better accuracy demonstrated in previous sections.

To evaluate HFP models in XBOIL using experimental data, it is necessary to express all bubble dynamics parameters as functions of wall superheat, since XBOIL takes wall superheat as input and predicts the corresponding heat flux. In the experimental dataset from Richenderfer et al., most bubble parameters (e.g. departure diameter, frequency, wait time, and growth time) are reported as functions of average heat flux, while nucleation site density is given as a function of wall superheat. To enable consistent use within XBOIL, the heat-flux-based parameters are interpolated as a function of the heat flux values using the boiling curves data and these are associated with the corresponding wall superheats. This allows direct computation of the HFP model components using experimentally measured bubble parameters as a function of wall superheat.

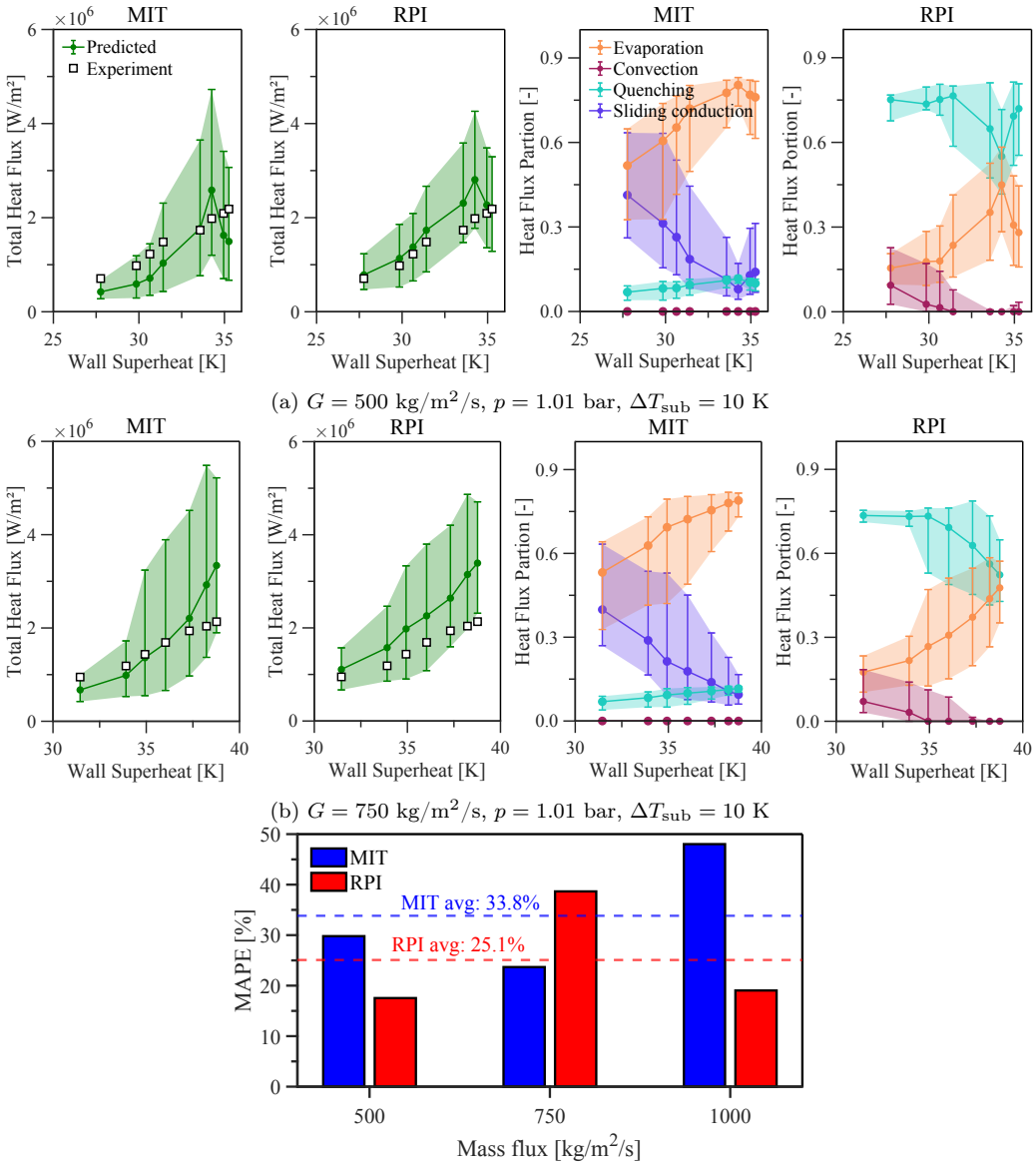

(a) $G = 500$ kg/m^2/s, $p = 1.01$ bar, $\Delta T_{\text{sub}} = 10$ K

(b) $G = 750$ kg/m^2/s, $p = 1.01$ bar, $\Delta T_{\text{sub}} = 10$ K

(c) mean-absolute percentage error.

Figure 15: Comparison of boiling curves, heat flux components and MAPE with the MIT and RPI heat flux partitioning models using experimental bubble parameters with two mass fluxes.

The uncertainties in the experimental bubble parameters are estimated by extracting the minimum and maximum bounds from the error bars shown in the figures of the Richenderfer et al. study. To account for the combined effect of these

uncertainties, a simultaneous variation approach is adopted. In this method, the minimum and maximum values of each parameter are used together to compute the lower and upper bounds of the predicted heat flux. This yields a conservative uncertainty envelope that reflects the compounded influence of experimental variability across all inputs. The nominal prediction corresponds to using the nominal values of all parameters, while the bounds represent the extreme cases where all parameters simultaneously assume their minimum or maximum values.

Figure 15 compares boiling curve predictions from the MIT and RPI heat flux partitioning models using experimentally measured bubble parameters for three different mass fluxes. Both models show reasonable agreement with experimental data, where for the most part, the experimental measurements are encapsulated within the predictive bounds. However, neither model consistently outperforms the other across all cases. This variability is reflected in the mean-absolute percentage error shown in Figure 15c, where RPI achieves a lower average MAPE of 25.1% compared to 33.8% for MIT.

More interestingly, despite being supplied with identical bubble dynamics inputs, the two HFP models predict vastly different heat flux components. In the MIT model, evaporation is the dominant heat transfer mechanism across most of the wall superheat range and it increases with superheat. The sliding conduction component is the next most significant, contributing substantially at low superheats but decreasing as the wall superheat rises. Quenching plays a minor role throughout, and the single-phase convection contribution is effectively negligible. In contrast, the RPI model assigns the largest portion of the heat flux to quenching across the entire superheat range, with evaporation as the second dominant mechanism. The convection component in RPI starts out more prominent at lower wall superheats but decreases noticeably with increasing superheat. Sliding conduction is not included in the RPI formulation and is therefore absent.

The contrasting heat flux decompositions observed between the RPI and MIT formulations reflect fundamental differences in how each framework conceptualises the spatial and temporal distribution of heat transfer at the wall. In the classical RPI approach, the total wall heat flux is partitioned into forced convection, quenching, and evaporation. The evaporation term is directly associated with the latent heat carried by departing bubbles and therefore scales with bubble volume, departure frequency, and nucleation site density. The quenching contribution represents transient conduction during post-departure rewetting and is evaluated over a prescribed bubble influence area, typically defined as a circular region proportional to $D_d^2 \overline{N}_b$ with an empirical area factor. In this formulation, the bubble life cycle is effectively reduced to departure-driven evaporation and subsequent boundary-layer redevelopment over

a geometrically defined influence zone.

In contrast, the MIT framework [17, 21], explicitly tracks additional mechanisms over the bubble ebullition cycle. Beyond forced convection and solid quenching, the MIT model introduces sliding-induced transient conduction as a distinct partition and incorporates microlayer evaporation as part of the evaporative contribution. Gilman et al. [21] emphasises that sliding bubbles and their wake-driven disruption of the thermal boundary layer are not represented in the RPI formulation, despite experimental evidence of their importance in subcooled flow boiling. Consequently, the MIT framework redistributes heat transfer mechanisms temporally (growth, sliding, departure) and spatially (footprint, sliding track, rewetting region), rather than confining transient conduction solely to post-departure quenching over a static influence area.

Variability in heat flux decomposition has also been reported in the literature; for example, Kim and Kim [26] showed that incorporating bubble coalescence modifies the relative evolution of quenching and evaporation area fractions in the RPI model, leading to markedly different component contributions despite being built upon the same underlying partitioning concept.

These contrasting patterns reveal that even when supplied with identical bubble parameter inputs, the MIT and RPI models encode fundamentally different assumptions about the dominant mechanisms of heat transfer. This further highlights the challenges in accurate modelling and physical representation of heat transfer in boiling flows. It demonstrates that model development will need to focus not only on the bubble parameter sub-models but also on the overarching heat flux partitioning formulation.

5. Conclusions

This work presented a comprehensive and systematic evaluation of heat flux partitioning (HFP) models and their associated bubble dynamics sub-models using a zero-dimensional, point-averaged framework implemented in MATLAB. Three HFP formulations were assessed in combination with multiple closures for key bubble dynamics parameters, including departure diameter, departure frequency, nucleation site density, growth and wait times, and single-phase convection, resulting in over 16,000 distinct model configurations. The framework was evaluated against an extensive database comprising both pool and flow boiling experiments covering wide ranges of pressure, subcooling, mass flux, and surface conditions.

The results demonstrated a substantial variability in predictive accuracy across the different HFP formulations and sub-model combinations. It was shown that it

is possible to match experimental heat flux prediction provided the 'right' combination of sub-models are selected for each test case, however no single configuration exhibited consistent accuracy across all datasets. This highlighted that model performance is dictated by compensatory interactions between multiple closures within the heat flux partitioning framework. For example, a less accurate departure diameter model can sometimes be offset by a nucleation site density or frequency model that over-predicts its respective contribution, yielding an overall heat flux that coincidentally aligns with experiments. This behaviour underscores a fundamental limitation of current HFP-based approaches: apparent agreement with experimental boiling curves does not necessarily indicate physically consistent predictions at the sub-model level. Consequently, efforts to improve boiling models must focus not only on refining individual correlations/models but also on ensuring their mutual consistency and physical compatibility across operating conditions.

Three levels of sensitivity analyses were performed to further examine model behaviour: (i) sensitivity to flow conditions, (ii) sensitivity of key modelling parameters such as contact angle, and (iii) sensitivity to alternative sub-model choices. These analyses highlighted the strong dependence of HFP predictions on both operating and modelling parameters, particularly at high pressures and large subcooling.

The analysis also provides insight into the limitations of current boiling closures when applied across diverse regimes. Many bubble dynamics correlations were originally developed from experiments conducted under relatively narrow operating conditions, which may contribute to the observed variability in predictive performance across the datasets considered here. In addition, several closures for bubble parameters are typically formulated independently, despite the strong physical coupling between the bubble parameters and heat transfer mechanisms. As emphasised by Dhir [71], nucleate boiling arises from multiple interacting subprocesses, and neglecting these interdependencies can lead to compensatory error effects. The pressure-tuned analysis further suggests that the relative performance of sub-model combinations varies with operating conditions, indicating that regime-aware formulations and stronger physical consistency between bubble dynamics closures may be important considerations for future model development.

A critical insight emerged from the focused evaluation of the HFP formulations using experimentally measured bubble dynamics parameters from Richenderfer et al. [18]. By directly supplying the experimental departure diameters, frequencies, growth and wait times, and nucleation site densities to the models, the uncertainties associated with sub-model closures were eliminated, allowing an isolated assessment of the HFP mechanisms themselves. The results showed that both the MIT and RPI formulations reproduced the experimental boiling curves within their uncertainty

bounds, yet neither consistently outperformed the other. More notably, despite being provided with identical bubble-scale inputs, the two models produced markedly different decompositions of the total heat flux. These contrasting behaviours underscore that the discrepancies in predicted heat fluxes are rooted not only in sub-model uncertainties but also in epistemic uncertainties in HFP formulations.

The findings presented in this work highlight the need for a paradigm shift in the development and validation of boiling models. Progress will require moving beyond isolated or empirically tuned sub-models toward physically consistent and interoperable closure sets that capture the coupled nature of bubble dynamic parameters and the heat transfer mechanisms. Ultimately, advancing the predictive capability of boiling models will depend not on the continual refinement of individual correlations, but on achieving coherence across the entire hierarchy of sub-models and their integration within multiphase CFD frameworks.

Nomenclature

A_{sl}	Bubble sliding area [-]
α	Thermal diffusivity [m^2 s^{-1}]
Ca	Capillary number [-]
Ca_0	Capillary number at 1 bar, $2.16 \times 10^{-4}(\Delta T_w)^{1.216}$ [-]
c_p	Specific heat capacity at constant pressure [J kg^{-1} K^{-1}]
D_d	Bubble departure diameter [m]
D_{dry}	Dry spot diameter [m]
D_{in}	Inception diameter [m]
D_{lo}	Lift-off diameter [m]
D_{ml}	Microlayer extension diameter [m]
f	Bubble departure frequency [s^{-1}]
f_{Darcy}	Darcy friction factor [-]
g	Gravitational acceleration [m s^{-2}]
h_c	Convective heat transfer coefficient [W m^{-2} K^{-1}]
h_{lv}	Latent heat of vapourisation [J kg^{-1}]
Ja	Jakob number [-]
K	Bubble growth constant [m s$^{-1/2}$]
k_l	Thermal conductivity of liquid [W m^{-1} K^{-1}]
ν_l	Kinematic viscosity of liquid [m^2 s^{-1}]
$\overline{N_b}$	Nucleation site density [m^{-2}]
Nu	Nusselt number [-]
P	Pressure [Pa]
Pr	Prandtl number [-]
q''	Total heat flux [W m^{-2}]
q''_c	Convective heat flux [W m^{-2}]
q''_q	Quenching heat flux [W m^{-2}]

q''_e	Evaporative heat flux [W m^{-2}]
q''_{sc}	Sliding conduction heat flux [W m^{-2}]
q''_{ml}	Microlayer heat flux [W m^{-2}]
q''_{in}	Inception heat flux [W m^{-2}]
R_g	Gas constant [J mol^{-1} K^{-1}]
Ra	Rayleigh number [-]
Re	Reynolds number
η	Thermal diffusivity [J m^{-3} K^{-1}]
ρ_l	Liquid density [kg m^{-3}]
ρ_v	Vapour density [kg m^{-3}]
σ	Surface tension [N m^{-1}]
S_{sl}	Fraction of heat surface area influenced by sliding bubbles [-]
t^*	Time needed to reform the thermal boundary layer [s]
t_g	Growth time [s]
t_w	Wait time [s]
T_l	Liquid temperature [K]
T_g	Gas temperature [K]
T_w	Wall temperature [K]
ΔT_{w}	Wall superheat [K]
ΔT_{sub}	Wall subcooling [K]
T_{sat}	Saturation temperature [K]
θ	Contact angle [rad]
δ_{ml}	Microlayer thickness [m]

Acknowledgement

This work was supported by the Engineering and Physical Sciences Research Council (EPSRC) award EP/X039927/1. The authors thank the anonymous reviewers for their constructive comments and suggestions, which helped improve the clarity and presentation of this work.

Declaration of competing interest

The authors declare that they have no known competing financial interests or personal relationships that could have appeared to influence the work reported in this paper.

Appendix

This section provides a brief description of the various models for heat flux partitioning and bubble dynamics parameters evaluated in the paper.

Table A1: Heat flux partitioning models used in the present work.

Name and description	Model equation(s)
RPI [25] • Canonical heat flux partitioning (HFP) model; foundation for many later extensions. • Splits wall heat flux into convection, quenching, and evaporation contributions. • Widely adopted in CFD boiling simulations.	$q'' = q_c'' + q_q'' + q_e'',$ $q_c'' = h_c \left(1 - \frac{\pi}{4} D_d^2 K \overline{N_b}\right)(T_w - T_l), \quad K = 4.8 \exp\left(-\frac{\mathrm{Ja}}{80}\right)$ [72], $q_q'' = t_w f \frac{\pi}{4} D_d^2 K \overline{N_b} \frac{2k_l (T_w - T_l)}{\sqrt{\pi t_w k_l}/\rho_l c_{p,l}},$ $q_e'' = \frac{\pi}{6} \rho_v h_{lv} D_d^3 f \overline{N_b}.$
MIT [17] • Mechanistic HFP framework developed for subcooled flow boiling heat transfer. • Partitions heat flux mechanisms into single phase convection, quenching, evaporation, and sliding conduction. • Validated against subcooled flow boiling experiments at various pressures, subcooling and mass fluxes.	$q'' = q_c'' + q_q'' + q_{sc}'' + q_e'',$ $q_e'' = q_{ml}'' + q_{in}'',$ $q_q'' = \rho_h c_{ph} \frac{2}{3} \pi \left(\frac{D_{\mathrm{in}}}{2}\right)^2 f \overline{N}_b \Delta T_h, \quad \Delta T_h = 2.0$ K[10], $q_c'' = (1 - S_{sl})\, h_c (\Delta T_w + \Delta T_{\mathrm{sub}}),$ $q_{sc}'' = \frac{k_l}{\sqrt{\pi \eta_l t^*}} S_{sl} (T_w - T_l),$ $q_{ml}'' = \rho_l h_{lv} f \overline{N_b} \left\{ \delta_{ml} D_{ml}^2 \frac{\pi}{12} \left[2 - \left(\left(\frac{D_{dry}}{D_{ml}}\right)^2 + \frac{D_{dry}}{D_{ml}} \right) \right] \right\},$

Continued on next page

Table A1 (*Continued*)

Name and description	Model equation(s)
	$q''_{in} = \frac{4}{3}\pi \left(\frac{D_{in}}{2}\right)^3 \rho_v h_{lv} f \overline{N_b},$
	$\frac{D_{dry}}{D_{ml}} = \max\left(0.1237\,\mathrm{Ca}^{-0.373}\sin\theta,\ 1\right),$
	$D_{in} = \frac{D_{dry}}{D_{ml}} D_d, \qquad D_{ml} = \frac{D_{in}}{2},$
	$\delta_{ml} = 4 \times 10^{-6} \sqrt{\frac{\mathrm{Ca}}{\mathrm{Ca}_0}}, \qquad S_{sl} = \min\left(1,\ A_{sl}\overline{N_b} t^* f\right),$
	$A_{sl} = \frac{1}{\sqrt{\overline{N_b}}} \left(\frac{D_{lo} + D_d}{2}\right), \quad t^* = \frac{k_l^2}{h_c \pi \eta_l}, \quad l_0 = 1.2 D_d.$
KIM AND KIM [26] • Extension of the RPI model. • Introduces correction factors ($C_{m,1}$ and $C_{m,2}$) to account for bubble coalescence effects. • Validated for pool boiling with water and FC-72 at atmospheric pressure.	$q'' = q''_c + q''_q + q''_e,$
	$q''_c = \frac{k_l}{\sqrt{\pi \alpha_l t_w}} \Delta T_\mathrm{w} \left[1 - \pi (K R_d)^2 \overline{N_b} C_{m,2}\right],$
	$q''_q = \frac{2k_l}{\sqrt{\pi \alpha_l t_w}} \Delta T_\mathrm{w} \left[\pi (K R_d)^2 \overline{N_b} C_{m,2} - \pi (R_d \sin\theta)^2 \overline{N_b} C_{m,1}\right],$
	$q''_e = \frac{5k_f}{2\sqrt{\nu t_d}} \Delta T_\mathrm{w} \left[\pi (R_d \sin\theta)^2 \overline{N_b} C_{m,1}\right],$

Continued on next page

Table A1 (*Continued*)

Name and description	Model equation(s)
	$$C_{m,1} = \begin{cases} 1, & (2R_d \le d_b) \\ 1 - 4\left(\frac{1}{\pi}\cos^{-1}\left(\frac{d_b}{2R_d}\right) \right. & \\ \quad \left. -\frac{d_b}{2\pi R_d}\sqrt{R_d^2 - \frac{d_b^2}{4}}\right), & (\sqrt{2}R_d \le d_b < 2R_d) \\ \frac{d_b^2}{\pi R_d^2}, & (d_b < \sqrt{2}R_d) \end{cases}$$ $$d_b = 1/\sqrt{N_b}, \qquad R_d = D_b/2,$$ $C_{m,2}$ is obtained by substituting KR_d in the equation for $C_{m,1}$.

Table A2: Departure diameter models used in the present work.

Name and description	Model equation(s)
BOVARD ET AL. [27] • Model developed based on experimental measurements from pool boiling with various liquids and heater surfaces. • Correlation based on force balance and estimated dimensionless numbers.	$$D_d = c_0\left[c_1 + \mathrm{Ja}^{c_2}\mathrm{Ca}^{c_3}\left(\frac{\alpha_f}{\alpha_s}\right)^{c_4}\right]\left[\frac{\sigma}{g(\rho_l - \rho_v)}\right]^{1/2},$$ $$c_0 = 17.952177, c_1 = 0.0172742, c_2 = 1.285607,$$ $$c_3 = 0.661205, c_4 = 0.025346.$$

Continued on next page

Table A2 (*Continued*)

Name and description	Model equation(s)
COLE [38] • Correlation developed based on experimental observations in pool boiling of water and organic liquids at atmospheric and sub-atmospheric pressures. • Model based on the influence of bubble growth rate (through the Jakob number), buoyancy and surface tension forces (similar to Fritz's model) on departure diameter.	$D_d = 0.04\mathrm{Ja}\sqrt{\dfrac{2\sigma}{g(\rho_l - \rho_v)}}$
COLE AND ROHSENOW [29] • Extension of the Cole model, by introducing the constant C, and the bubble size dependence on the modified Jakob number. • Based on pool boiling for water and other liquids at low pressure.	$D_d = C\mathrm{Ja}^{5/4}\left[\dfrac{2\sigma g_c}{g(\rho_l - \rho_v)}\right]^{1/2},$ $C = 1.5 \times 10^{-4}$ for water, $C = 4.65 \times 10^{-4}$ for other fluids.
COLOMBO AND FAIRWEATHER [23] • A mechanistic model, based on the balance of forces acting on a bubble at the nucleation site (based on the work of Klausner et al. [22]). • Forces considered are surface tension, quasi-steady drag, buoyancy, shear lift, unsteady drag, hydrodynamic and contact pressure. • New formulation for bubble growth rate accounting for microlayer evaporation under the bubble. • Validated primarily for nucleate flow boiling data from experiment with water and R-113 with a maximum pressure of 5 bar.	$\sum F_x = F_{stx} + F_{qsd} + F_b \sin\theta + F_{udx} = 0,$ $\sum F_y = F_{sty} + F_{sl} + F_b \cos\theta + F_{udy} + F_p + F_{cp} = 0,$ $\dfrac{dR(t)}{dt} = \dfrac{1}{C_2}\mathrm{Pr}^{-0.5}\mathrm{Ja}\left(\dfrac{k_l}{\rho_l c_{p,l}}\right)^{0.5} t^{-0.5}$ $+ \sqrt{\dfrac{3}{\pi}} k_l (T - T_{sat})\left(\dfrac{k_l}{\rho_l c_{p,l}}\right)^{0.5} (1-b)t^{-0.5}$ $- \dfrac{h_c}{\rho_v h_{lv}}(T_{sat} - T_{sub})b.$

Continued on next page

Table A2 (*Continued*)

Name and description	Model equation(s)
FRITZ [30] • One of the earliest correlations, inspiring many other correlations, developed by accounting for the force balance between buoyancy and surface tension forces. • Shown to have limited accuracy beyond atmospheric pressure e.g. [32].	$D_d = 0.0208\theta\sqrt{\dfrac{\sigma}{g(\rho_l - \rho_v)}}$
GOLORIN ET AL. [31] • Correlation based on pool boiling data for ethyl alcohol (at pressures, $P = 1 - 15$ bar) and benzene (at $P = 0.66 - 34$ bar).	$D_d = \dfrac{0.0099\sigma}{g(\rho_l - \rho_v)} + \left\{ \left[\dfrac{15.6\rho_l}{g(\rho_l - \rho_v)} \right]^{1/3} [0.6\alpha_l \mathrm{Ja}] \right\}$
KOCAMUSTAFAOGULLARI [32] • Based on the Fritz model, but arguing the empirical correlation should include the strong pressure dependence on the departure diameter. • Extended based on pool boiling experiments of water at a wider range of pressures, $0.067 \leq P \leq 141.87$ bar.	$D_d = 2.64 \times 10^{-5} \left[\dfrac{\sigma}{g(\rho_l - \rho_v)} \right]^{1/2} \left(\dfrac{\rho_l - \rho_v}{\rho_l} \right)^{0.9}$
MIT [17] • Developed based on experimental measurements of departure diameter in subcooled flow boiling of water at various flow conditions. • Correlation leverages experimental trends of bubble departure with superheat, subcooling and velocity, and performs a model fitting.	$D_d = 18.9 \times 10^{-6} \left(\dfrac{\rho_l - \rho_v}{\rho_v} \right)^{0.27} \mathrm{Ja}_{\mathrm{sup}}^{0.75} \times (1 + \mathrm{Ja}_{\mathrm{sub}})^{-0.3} (\mathrm{vel})^{-0.26}$

Continued on next page

Table A2 (*Continued*)

Name and description	Model equation(s)
NAM ET AL. [33] • Correlation developed based pool boiling of water at atmospheric pressure on superhydophilic surfaces and the increased importance of the contact angle on the bubble departure diameter. • Similar to the Fritz model, new correlation based on the balance on buoyancy and surface tension forces.	$D_d = \sqrt{\frac{24(\sin\theta)^2}{2+3\cos\theta-(\cos\theta)^3}}\left[\frac{\sigma}{g(\rho_l-\rho_v)}\right]^{1/2}$
PHAN ET AL. [34] • Correlation accounting for the effect of contact angle on bubble growth based on the concept of macro- and micro-contact angles. • Correlation does not account for the effects of superheat and subcooling. • Only applicable to bubbles detaching upwards from a horizontal surface.	$D_d = \left(6\sqrt{\frac{3}{2}}\right)^{1/3}\left(\frac{\rho_l}{\rho_v}\right)^{-1/2}\left(\frac{\rho_l}{\rho_v}-1\right)^{1/3}\times \tan\theta^{-1/6}\left[\frac{\sigma}{g(\rho_l-\rho_v)}\right]^{1/2}$
RUCKENSTEIN [35, 73] • Model based on force balance between buoyancy and drag forces. • Modified version of the Cole model that includes thermal diffusivity and the Jakob number.	$D_d = \left[\frac{3\pi^2\rho_l\alpha_l^2 g^{0.5}(\rho_l-\rho_v)^{0.5}}{\sigma^{3/2}}\right]\mathrm{Ja}^{4/3}\left[\frac{2\sigma}{g(\rho_l-\rho_v)}\right]^{1/2}$

Continued on next page

Table A2 (*Continued*)

Name and description	Model equation(s)
TOLUBINSKY AND KOSTANCHUK [74] • Simple empirical correlation based on subcooled flow boiling experiments with water. • Experimental operating conditions ranges: $1 \leq P \leq 10$ bar, $5 \leq T_{\text{sub}} \leq 60$ °C, and $0.08 \leq u \leq 0.2$ m/s.	$D_d = \min\left(0.0014, 0.0006 \exp\left(-\dfrac{\Delta T_{\text{sub}}}{45}\right)\right)$
VAN STRALEN AND ZIJL [75] • Modified version of the Cole model that includes thermal diffusivity and the Jakob number.	$D_d = 2.63\left(\dfrac{\text{Ja}\alpha_l^2}{g}\right)^{1/3}\left[1+\left(\dfrac{2\pi}{3\text{Ja}}\right)^{0.5}\right]^{1/4}$

Table A3: Departure frequency models assessed in the present work.

Name and description	Model equation(s)
EXACT e.g. [76] • Based on experimental observations (e.g. Jakob and Linke [77]). • Require models for the growth (t_g) and wait (t_w) times.	$f = \dfrac{1}{t_g + t_w}$

Continued on next page

Table A3 (*Continued*)

Name and description	Model equation(s)
COLE [38] • Formulated alongside the Cole departure diameter model based on pool boiling experiments. • Correlation derived based on dimensional analysis and regression on bubble dynamics experimental data.	$$fD_d^{1/2} = \left[\frac{4g(\rho_l - \rho_v)}{3\rho_l}\right]^{1/2}$$
PEEBLES AND GARBER [39] • One of the early models, relating the departure frequency to the bubble growth and wait times. • Some other models, such as Cole's, avoid explicitly correlating to wait and growth times due to measurement difficulties at the time the correlations were being developed.	$$fD_d = 1.18\left[\frac{t_g}{t_g + t_w}\right]\left[\frac{\sigma g(\rho_l - \rho_v)}{\rho_l^2}\right]^{1/4}$$
SAKASHITA AND ONO [40] • Correlation developed based on high-pressure pool boiling experiments of water. • Formulation based on force-balance considering buoyancy and drag forces.	$$f = 0.6\left[\frac{g(\rho_l - \rho_v)}{\rho_l}\right]^{2/3}\left\{\nu_l\left[\frac{g(\rho_l - \rho_v)\rho_l^2\nu_l^4}{\sigma^3}\right]^{-0.25}\right\}^{-1/3}$$
STEPHAN [41] • Correlation relating departure frequency to the bubble departure diameter, liquid density, surface tension and acceleration due to gravity.	$$fD_d = \frac{1}{\pi}\left[\frac{g}{2}\left(D_d + \frac{4\sigma}{\rho_l g D_d}\right)\right]^{1/2}$$

Continued on next page

Table A3 (*Continued*)

Name and description	Model equation(s)
ZUBER [42] • Similar to correlations by Cole and Peebles and Gaber, the correlation uses the observation (based on Jakob and Linke experiments for pool boiling [77]) that the product of frequency and bubble diameter is governed by a buoyancy-inertia scaling and remains a constant for a given nucleation site.	$$fD_d = \left(\frac{1.18}{2}\right)\left[\frac{\sigma g(\rho_l - \rho_v)}{\rho_l^2}\right]^{1/4}$$

Table A4: Nucleation site density models assessed in the present work.

Name and description	Model equation(s)
HIBIKI AND ISHII (HI) [43] • Mechanistic model expressing the nucleation site density as a function of wall superheat, pressure, critical cavity size and contact angle. • Based on the argument that there are cavities distributed on the heater surface which are activated based on the flow conditions and fluid properties. • Validated against data for pool and flow boiling. Model application range: $0 \leq G \leq 886$ kg/m^2/s, $1.01 \leq P \leq 198$ bar, and $5^\circ \leq \theta \leq 90^\circ$.	$$\overline{N_b} = N_0\left(1 - \exp\left(-\frac{\theta^2}{8\mu^2}\right)\right)\left[\exp\left(\frac{f(\rho^+)\lambda'}{R_c}\right) - 1\right],$$ $$R_c = \frac{2\sigma[1 + (\rho_v/\rho_l)]/P}{\exp\left[h_{lv}(T_g - T_{\text{sat}})/(R_g T_g T_{\text{sat}})\right] - 1},$$ $$\rho^+ = \log\left(\frac{\rho_l - \rho_v}{\rho_v}\right),$$ $$f(\rho^+) = -0.01064 + 0.48246\rho^+ - 0.22712(\rho^+)^2 + 0.05468(\rho^+)^3,$$ $N_0 = 4.72 \times 10^5$ sites/m^2, $\mu = 0.722$ rad, $\lambda' = 2.56 \times 10^{-6}$ m.

Continued on next page

Table A4 (*Continued*)

Name and description	Model equation(s)
HIBIKI AND ISHII MIT [10, 17, 21] • The Hibiki and Ishii model may predict unphysically high number of nucleation sites due to the exponential relationship of the wall superheat to $\overline{N}_b$ [45]. At high pressures, this can also lead to convergence issues in CFD simulations [17, 21]. • The MIT modification uses a statistical approach based on complete spatial randomness theory.	$\overline{N_b} = \begin{cases} \overline{N_b}_{\mathrm{HI}}, & N_0\overline{N_b}_{\mathrm{HI}} < e^{-1} \\ \dfrac{0.2689 N_0 \overline{N_b}_{\mathrm{HI}} + 0.2690}{N_0}, & e^{-1} \le N_0\overline{N_b}_{\mathrm{HI}} \le e \\ \dfrac{\ln(N_0\overline{N_b}_{\mathrm{HI}}) - \ln(\ln(N_0\overline{N_b}_{\mathrm{HI}}))}{N_0}, & N_0\overline{N_b}_{\mathrm{HI}} > e \end{cases}$ $N_0 = f t_g \overline{N_b}_{\mathrm{HI}}$
LEMMERT AND CHAWLA [44] • One of the most commonly used models in CFD simulations due to simplicity and good numerical convergence characteristics. • Correlation based on experimental data from flow boiling of coolant (R11) with a pressure range of 1-2 bar.	$\overline{N_b} = (185\Delta T_w)^{1.805}$

Continued on next page

Table A4 (*Continued*)

Name and description	Model equation(s)
LI ET AL. [45] • Correlation developed on parametric analysis of existing experimental data. • Formulates the nucleation site density as a function of the wall superheat, contact angle, and pressure. • Model includes effects of the variation of contact angle with changes in wall temperature. • Authors suggest same range of application as the Hibiki and Ishii model. Only applicable when the working fluid is water.	$\overline{N_b} = N_0 \cdot (1 - \cos\theta_0) \left(\frac{T_c - T_{\text{sat}}}{T_c - T_0}\right)^{\gamma}$ $\times \exp(f(P)) \cdot \Delta T_w^{A \cdot \Delta T_w + B}$, $f(P) = 26.006 - 3.678\exp(-2P) - 21.907$ $\exp\left(-\frac{P}{24.065}\right)$, $A = -0.0002P^2 + 0.0108P + 0.0119$, $B = 0.122P + 1.988$, P in MPa, $N_0 = 10^3$ sites/m^2, $\theta_0 = 41.37°$, $T_c = 374$ K, $T_0 = 25$, $\gamma = 0.719$.
WANG AND DHIR [46] • Correlation based on experimental data from pool boiling of water at atmospheric pressure. • Expresses the nucleation site density as a function of contact angle and the critical cavity diameter.	$\overline{N_b} = 5.0 \times 10^9 (1 - \cos\theta) D_c^{-6.0}$ $D_c = \frac{4\sigma T_{\text{sat}}}{\rho_v h_{lv} \Delta T_w} \times 10^6$

Continued on next page

Table A4 (*Continued*)

Name and description	Model equation(s)
YANG ET AL. [47] • Empirical correlation developed based on subcooled flow boiling experiments of water in a vertical upward narrow rectangular channel at atmospheric pressure. • Experimental conditions: $G = 122-657$ kg/m^2/s and $T_{sub} = 4.7 - 33.3$ °C. • Model valid for $\Delta T_{sup} < 12$ °C in the nucleate boiling regime.	$\overline{N_b} = 1 \times 10^4 \left(0.28 \Delta T_w^{2.66}\right)$

Table A5: Bubble growth and wait times models assessed in the present work.

Name and description	Model equation(s)
GROWTH TIME	
LEE ET AL. [48] • Correlation based on saturated pool boiling experiments using R11 and R113 at atmospheric pressure. • Model formulated using dimensional analysis and scaling parameters based on the experimental data.	$t_g = 67.5 \mathrm{Ja} \alpha_l \rho_l \dfrac{D_d}{\sigma}$

Continued on next page

Table A5 (*Continued*)

Name and description	Model equation(s)
MIT [17] • Formulated based on a new model for the bubble growth rate that accounts for heat transfer from the bulk flow and microlayer evaporation. • Parameters for the bubble growth rate constant, K, tuned on experimental measurements of bubble departure diameters for flow and pool boiling data at various pressures, subcoolings and velocities.	$t_g = \left(\frac{D_d}{4K}\right)^2$, $K = \mathrm{Ja}_{\mathrm{sup}}\sqrt{\eta_f}\left(\frac{1.243}{\sqrt{\mathrm{Pr}_f}} - \min\left(0.5\frac{1.243}{\sqrt{\mathrm{Pr}_f}}, 0.0977\frac{\Delta T_{\mathrm{sub}}}{\Delta T_{\mathrm{w}}}\right)\right)$ [10]
VAN STRALEN ET AL.[37] • Based on growth rate equation from first-principles coupling of momentum and energy conservation in a liquid-vapour system.	$t_g = \frac{1}{\alpha_l}\left(\frac{D_d F_f}{2.26 F_{\mathrm{wall}}\mathrm{Ja}}\right)^2$, $\frac{F_f}{F_{\mathrm{wall}}} = \frac{(k_l\rho_l c_{p,l})^{1/2}}{(k_h\rho_h c_{p,h})^{1/2}}$.
WAIT TIME	
MIT [17] • Correlation developed using regression on bubble departure frequency data from literature. Experiments were for subcooled flow boiling, with water and Novec-7000 for the working fluids, at atmospheric pressure. • Model does not account for the effect of flow velocity and wettability, due to lack of data.	$t_w = \frac{0.0061\mathrm{Ja}_{\mathrm{sub}}^{0.63}}{\Delta T_w}$

Continued on next page

Table A5 (*Continued*)

Name and description	Model equation(s)
VAN STRALEN ET AL. [37] • This is an approximate for wait time, based on analytical thermal recovery analysis in [37] and experimental observations.	$t_w = 3t_g$

Table A6: Nusselt number correlations used for calculating the single-phase heat transfer in the present work.

Name and description	Model equation(s)
CHURCHILL AND CHU [49] • Empirical correlation for natural convection in laminar and turbulent regimes, applicable to vertical surface or horizontal cylinder at a range of Prandtl and Rayleigh numbers.	$\mathrm{Nu} = \left\{ \frac{0.825 + 0.387\mathrm{Ra}^{1/6}}{[1 + (0.492/\mathrm{Pr})^{9/16}]^{8/27}} \right\}^2$
GNIELINSKI [50] • Empirical correlation for fully developed turbulent and transition flows in pipes. • Range of validity: $2300 < \mathrm{Re} < 10^6$ and $0.6 < \mathrm{Pr} < 10^5$.	$\mathrm{Nu} = \frac{(f_{\mathrm{Darcy}}/8)(\mathrm{Re}_D - 1000)\mathrm{Pr}}{1 + 12.7\sqrt{f_{\mathrm{Darcy}}/8}(\mathrm{Pr}^{2/3} - 1)}$

References

[1] M. Wu, J. Zhang, N. Gui, Q. Zou, X. Yang, J. Tu, S. Jiang, Z. Liu, Advances in the modeling of multiphase flows and their application in nuclear engineering—a review, Experimental and Computational Multiphase Flow 6 (2024) 287–352.

[2] N. Mérigoux, Multiphase Eulerian-Eulerian CFD supporting the nuclear safety demonstration, Nuclear Engineering and Design 397 (2022) 111914.

[3] A. Shynybayeva, L. R. Rojas-Solórzano, Eulerian–Eulerian modeling of multiphase flow in horizontal annuli: Current limitations and challenges, Processes 8 (2020) 1426.

[4] G. H. Yeoh, J. Tu, Computational techniques for multiphase flows, Butterworth-Heinemann, 2019.

[5] R. T. Lahey Jr, E. Baglietto, I. A. Bolotnov, Progress in multiphase computational fluid dynamics, Nuclear Engineering and Design 374 (2021) 111018.

[6] G. R. Warrier, V. K. Dhir, Heat transfer and wall heat flux partitioning during subcooled flow nucleate boiling—a review, Journal of Heat Transfer 128 (2006) 1243–1256.

[7] R. L. Mohanty, M. K. Das, A critical review on bubble dynamics parameters influencing boiling heat transfer, Renewable and Sustainable Energy Reviews 78 (2017) 466–494.

[8] M. Colombo, M. Fairweather, Accuracy of Eulerian–Eulerian, two-fluid CFD boiling models of subcooled boiling flows, International Journal of Heat and Mass Transfer 103 (2016) 28–44.

[9] G. Giustini, Modelling of boiling flows for nuclear thermal hydraulics applications—a brief review, Inventions 5 (2020) 47.

[10] M. Pham, G. Bois, F. Francois, E. Baglietto, Assessment of state-of-the-art multiphase CFD modeling for subcooled flow boiling in reactor applications, Nuclear Engineering and Design 411 (2023) 112379.

[11] C. S. Brooks, T. Hibiki, Modeling and validation of interfacial area transport equation in subcooled boiling flow, Journal of Nuclear Science and Technology 53 (2016) 1192–1204.

[12] M. Colombo, R. Rzehak, M. Fairweather, Y. Liao, D. Lucas, Benchmarking of computational fluid dynamic models for bubbly flows, Nuclear Engineering and Design 375 (2021) 111075.

[13] M. Colombo, M. Fairweather, RANS simulation of bubble coalescence and break-up in bubbly two-phase flows, Chemical Engineering Science 146 (2016) 207–225.

[14] M. Colombo, M. Fairweather, Influence of multiphase turbulence modelling on interfacial momentum transfer in two-fluid Eulerian-Eulerian CFD models of bubbly flows, Chemical Engineering Science 195 (2019) 968–984.

[15] G. Bois, P. Fillion, F. François, A. Burlot, A. B. H. Ali, A. Khaware, J. Sanyal, M. Rehm, B. Farges, F. Vinauger, et al., Benchmark DEBORA: Assessment of MCFD compared to high-pressure boiling pipe flow measurements, International Journal of Multiphase Flow 179 (2024) 104920.

[16] J. Garnier, E. Manon, G. Cubizolles, Local measurements on flow boiling of refrigerant 12 in a vertical tube, Multiphase Science and Technology 13 (2001).

[17] R. Kommajosyula, Development and assessment of a physics-based model for subcooled flow boiling with application to CFD, Ph.d. thesis, Massachusetts Institute of Technology, 2020.

[18] A. Richenderfer, A. Kossolapov, J. H. Seong, G. Saccone, E. Demarly, R. Kommajosyula, E. Baglietto, J. Buongiorno, M. Bucci, Investigation of subcooled flow boiling and CHF using high-resolution diagnostics, Experimental Thermal and Fluid Science 99 (2018) 35–58.

[19] M. J. Inanlu, V. Ganesan, N. V. Upot, C. Wang, Z. Suo, K. Fazle Rabbi, P. Kabirzadeh, A. Bakhshi, W. Fu, T. S. Thukral, et al., Unveiling the fundamentals of flow boiling heat transfer enhancement on structured surfaces, Science Advances 10 (2024) eadp8632.

[20] V. Voulgaropoulos, G. M. Aguiar, C. Markides, M. Bucci, Simultaneous laser-induced fluorescence, particle image velocimetry and infrared thermography for the investigation of the flow and heat transfer characteristics of nucleating vapour bubbles, International Journal of Heat and Mass Transfer 187 (2022) 122525.

[21] L. Gilman, E. Baglietto, A self-consistent, physics-based boiling heat transfer modeling framework for use in computational fluid dynamics, International Journal of Multiphase Flow 95 (2017) 35–53.

[22] J. F. Klausner, R. Mei, D. Bernhard, L. Zeng, Vapor bubble departure in forced convection boiling, International journal of heat and mass transfer 36 (1993) 651–662.

[23] M. Colombo, M. Fairweather, Prediction of bubble departure in forced convection boiling: A mechanistic model, International Journal of Heat and Mass Transfer 85 (2015) 135–146.

[24] G. Yang, W. Zhang, M. Binama, J. Sun, W. Cai, Review on bubble dynamic of subcooled flow boiling-part a: Research methodologies, International Journal of Thermal Sciences 184 (2023).

[25] N. Kurul, M. Z. Podowski, Multidimensional effects in forced convection subcooled boiling, in: Proceeding of International Heat Transfer Conference 9, Begellhouse, 1990.

[26] M. Kim, S. J. Kim, A mechanistic model for nucleate pool boiling including the effect of bubble coalescence on area fractions, International Journal of Heat and Mass Transfer 163 (2020) 120453.

[27] S. Bovard, H. Asadinia, G. Hosseini, S. A. Alavi Fazel, Investigation and experimental analysis of the bubble departure diameter in pure liquids on horizontal cylindrical heater, Heat and Mass Transfer 53 (2016).

[28] R. Cole, A photographic study of pool boiling in the region of the critical heat flux, AIChE Journal 6 (1960) 533–538.

[29] R. Cole, W. M. Rohsenow, Correlation of bubble departure diameters for boiling of saturated liquids, in: Chemical Engineering Progress Symposium Series, volume 65, 1969, pp. 211–213.

[30] W. Friz, Maximum volume of vapor bubbles, Physikalische Zeitschrift 36 (1935) 379–354.

[31] V. S. Golorin, B. A. Kol'chugin, E. A. Zakharova, Investigation of the mechanism of nucleate boiling of ethyl alcohol and benzene by means of high-speed motion-picture photography, Heat Transfer - Soviet Research 10 (1978) 79–98.

[32] G. Kocamustafaogullari, Pressure dependence of bubble departure diameter for water, International Communications in Heat and Mass Transfer 10 (1983) 501–509.

[33] Y. Nam, E. Aktinol, V. K. Dhir, Y. S. Ju, Single bubble dynamics on a superhydrophilic surface with artificial nucleation sites, International Journal of Heat and Mass Transfer 54 (2011) 1572–1577.

[34] H. T. Phan, N. Caney, P. Marty, S. Colasson, J. Gavillet, A model to predict the effect of contact angle on the bubble departure diameter during heterogeneous boiling, International Communications in Heat and Mass Transfer 37 (2010) 964–969.

[35] R. Ruckenstein, Recent trends in boiling heat transfer research, Applied Mechanics Reviews 17 (1964) 663–672.

[36] V. I. Tolubinsky, D. Kostanchuk, Vapour bubbles growth rate and heat transfer intensity at subcooled water boiling, in: Proceeding of International Heat Transfer Conference 4, Begellhouse, 1970.

[37] S. van Stralen, M. Sohal, R. Cole, W. Sluyter, Bubble growth rates in pure and binary systems: Combined effect of relaxation and evaporation microlayers, International Journal of Heat and Mass Transfer 18 (1975) 453–467.

[38] R. Cole, Bubble frequencies and departure volumes at subatmospheric pressures, AIChE Journal 13 (1967) 779–783.

[39] F. N. Peebles, H. J. Garber, Studies on the motion of gas bubbles in liquids, Chemical Engineering Progress 49 (1953) 88–97.

[40] H. Sakashita, A. Ono, Boiling behaviors and critical heat flux on a horizontal plate in saturated pool boiling of water at high pressures, International Journal of Heat and Mass Transfer 52 (2009) 744–750.

[41] K. Stephan, Enhancement of heat transfer during boiling, in: Heat Transfer in Condensation and Boiling, Springer, 1992, pp. 292–301.

[42] N. Zuber, Nucleate boiling. the region of isolated bubbles and the similarity with natural convection, International Journal of Heat and Mass Transfer 6 (1963) 53–78.

[43] T. Hibiki, M. Ishii, Active nucleation site density in boiling systems, International Journal of Heat and Mass Transfer 46 (2003) 2587–2601.

[44] M. Lemmert, L. M. Chawla, Influence of flow velocity on surface boiling heat transfer coefficient, International Heat Transfer Conference Proceedings (1974). Published in 1977.

[45] Q. Li, Y. Jiao, M. Avramova, P. Chen, J. Yu, J. Chen, J. Hou, Development, verification and application of a new model for active nucleation site density in boiling systems, Nuclear Engineering and Design 328 (2018) 1–9.

[46] C. H. Wang, V. K. Dhir, Effect of surface wettability on active nucleation site density during pool boiling of water on a vertical surface, ASME Journal of Heat Transfer 115 (1993) 659–669.

[47] L. X. Yang, A. Guo, D. Liu, Experimental investigation of subcooled vertical upward flow boiling in a narrow rectangular channel, Experimental Heat Transfer 29 (2014) 221–243.

[48] H. C. Lee, B. D. Oh, S. W. Bae, M. H. Kim, Single bubble growth in saturated pool boiling on a constant wall temperature surface, International Journal of Multiphase Flow 29 (2003) 1857–1874.

[49] S. W. Churchill, H. H. S. Chu, Correlating equations for laminar and turbulent free convection from a vertical plate, International Journal of Heat and Mass Transfer 18 (1975) 1323–1329.

[50] V. Gnielinski, New equations for heat and mass transfer in turbulent pipe and channel flow, International Chemical Engineering 16 (1976) 359–368.

[51] I. H. Bell, J. Wronski, S. Quoilin, V. Lemort, Pure and pseudo-pure fluid thermophysical property evaluation and the open-source thermophysical property library coolprop, Industrial & Engineering Chemistry Research 53 (2014) 2498–2508.

[52] B. A. Phillips, Experimental investigation of subcooled flow boiling using synchronized high speed video, infrared thermography, and particle image velocimetry, Ph.D. thesis, Massachusetts Institute of Technology, 2014.

[53] A. J. Richenderfer, Experimental study of heat flux partitioning in pressurized subcooled flow boiling, Ph.D. thesis, Massachusetts Institute of Technology, 2018.

[54] W. Chen, Y. Lee, D. Groeneveld, Measurement of boiling curves during rewetting of a hot circular duct, Int. J. Heat Mass Transfer;(United Kingdom) 22 (1979).

[55] W. E. Kennel, Local boiling of water and superheating of high pressure steam in annuli, Ph.D. thesis, Massachusetts Institute of Technology, 1949.

[56] D. Lee, B. Elward, P. Brooks, R. Umretiya, J. Rojas, M. Bucci, R. B. Rebak, M. Anderson, Enhanced flow boiling heat transfer on chromium coated zircaloy-4 using cold spray technique for accident tolerant fuel (atf) materials, Applied Thermal Engineering 185 (2021) 116347.

[57] J. H. Seong, C. Wang, B. Phillips, M. Bucci, Effect of pvd-coated chromium on the subcooled flow boiling performance of nuclear reactor cladding materials, Applied Thermal Engineering 213 (2022) 118670.

[58] V. Morozov, Heat transfer during the boiling of water in tubes, Convective Heat Transfer in Two Phase and One Phase Flows (1969) 106–114.

[59] N. Basu, G. R. Warrier, V. K. Dhir, Wall heat flux partitioning during subcooled flow boiling: part ii—model validation, J. Heat Transfer 127 (2005) 141–148.

[60] W. M. Rohsenow, J. A. Clark, Heat transfer and pressure drop data for high heat flux densities to water at high subcritical pressures, Technical Report, Cambridge, Mass.: MIT Division of Industrial Cooperation, 1951, 1951.

[61] Y. Lie, T. Lin, Subcooled flow boiling heat transfer and associated bubble characteristics of r-134a in a narrow annular duct, International journal of heat and mass transfer 49 (2006) 2077–2089.

[62] B. Vadgama, D. K. Harris, Measurements of the contact angle between r134a and both aluminum and copper surfaces, Experimental Thermal and Fluid Science 31 (2007) 979–984.

[63] C. Gerardi, J. Buongiorno, L.-w. Hu, T. McKrell, Study of bubble growth in water pool boiling through synchronized, infrared thermometry and high-speed video, International Journal of Heat and Mass Transfer 53 (2010) 4185–4192.

[64] J. Kim, S. Jun, R. Laksnarain, S. M. You, Effect of surface roughness on pool boiling heat transfer at a heated surface having moderate wettability, International Journal of Heat and Mass Transfer 101 (2016) 992–1002.

[65] Y. Chang, Y. Ferng, Experimental investigation on bubble dynamics and boiling heat transfer for saturated pool boiling and comparison data with previous works, Applied Thermal Engineering 154 (2019) 284–293.

[66] R. Benjamin, A. Balakrishnan, Nucleate pool boiling heat transfer of pure liquids at low to moderate heat fluxes, International Journal of Heat and Mass Transfer 39 (1996) 2495–2504.

[67] H. Kurihara, J. Myers, The effects of superheat and surface roughness on boiling coefficients, AIChE Journal 6 (1960) 83–91.

[68] S. Dahariya, A. R. Betz, High pressure pool boiling: Mechanisms for heat transfer enhancement and comparison to existing models, International Journal of Heat and Mass Transfer 141 (2019) 696–706.

[69] V. P. Carey, Influence of system pressure on microlayer evaporation during nucleate boiling, Journal of Heat Transfer 100 (1978) 49–56.

[70] K. Ardron, G. Giustini, S. Walker, Prediction of dynamic contact angles and bubble departure diameters in pool boiling using equilibrium thermodynamics, International Journal of Heat and Mass Transfer 114 (2017) 1274–1294.

[71] V. K. Dhir, Mechanistic prediction of nucleate boiling heat transfer—achievements and challenges, Journal of Heat Transfer 128 (2006) 1–12. doi:10.1115/1.2136953.

[72] J. Tu, G. Yeoh, On numerical modelling of low-pressure subcooled boiling flows, International Journal of Heat and Mass Transfer 45 (2002) 1197–1209.

[73] E. Ruckenstein, A physical model for nucleate boiling heat transfer, International Journal of Heat and Mass Transfer 7 (1964) 191–198.

[74] V. Tolubinsky, D. Kostanchuk, Vapour bubbles growth rate and heat transfer intensity at subcooled water boiling, in: International Heat Transfer Conference 4, volume 23, Begel House Inc., 1970.

[75] S. J. D. van Stralen, W. Zijl, Fundamental developments in bubble dynamics, in: Proceedings of the 6th International Heat Transfer Conference, 1978.

[76] C. S. Brooks, T. Hibiki, Wall nucleation modeling in subcooled boiling flow, International Journal of Heat and Mass Transfer 86 (2015) 183–196.

[77] M. Jakob, W. Linke, Der wärmeübergang von einer waagerechten platte an siedendes wasser, Forschung auf dem Gebiet des Ingenieurwesens A 4 (1933) 75–81.